Simulation research on aerodynamic noise characteristics of a compressor under different working conditions

Huabing Lu [1,2], Youhong Xiao [1,a], Yiteng Huang[a], Zhigang Liu [1], Ye Yuan [1], Peilin Zhou [2,b] Guanghui Yang [1]

[1] College of Power and Energy Engineering, Harbin Engineering University, Harbin, Heilongjiang Province 150001, China.

[2] Department of Naval Architecture and Marine Engineering, University of Strathclyde, Glasgow G1 1XQ, United Kingdom.

ABSTRACT

The shear stress transport turbulence model is employed to conduct a detailed study of flow characteristics at the highest efficiency point and the near-stall point in a full-channel 1.5-stage compressor in this paper. The simulation results for the compressor's total pressure ratio and efficiency exhibit good agreement with experimental data. Emphasis is placed on examining the internal flow structure in the tip area of the

[a] Youhong Xiao Email: xiaoyouhong@hrbeu.edu.cn

[b] Peilin Zhou Email: Peilin.zhou@Strath.ac.uk

This is a peer-reviewed, version of record of the following paper: Lu, H., Xiao, Y., Huang, Y., Liu, Z., Yuan , Y., Zhou, P., & Yang , G. (2024). Simulation research on aerodynamic noise characteristics of a compressor under different working conditions. Journal of the Acoustical Society of America, 155(4), 2517–2537. https://doi.org/10.1121/10.0025470

compressor rotor under near-stall conditions. The results reveal that significant differences in flow structure primarily occur in the tip area as the compressor approaches stall. Specifically, a reduction in turbulent kinetic energy is observed in a region spanning approximately 20% to 60% of the chord length on the rotor suction face near stall conditions. Two additional peak frequencies, at 0.8 and 1.6 times the Blade Passage Frequency (BPF), are observed, and the intricate flow phenomena are elaborated at the near-stall point. The near-stall point exhibits greater noise levels than the highest efficiency point, with the intensity of the surface source increasing by more than 10 dB, peaking at 20 dB. This additional peak serves as a significant supplementary noise source near the stall point, leading to a maximum increase of 33.3 dB in the free radiated sound power. The acoustic response within the duct indicates that the compressor operating at the near-stall point continues to produce substantial noise on the actual test bench, showing an average increase of 6 dB in noise levels, and the distribution of the additional peak single-tone noise at the entrance significantly differs from that observed at the highest efficiency point.

Keywords： Compressor; Aerodynamic noise; Highest efficiency; Near-stall; Flow characteristics

I. INTRODUCTION

Gas turbines widely employed in maritime transportation and thermal power generation consist of three core components, with the compressor being one of them. The maritime compressor exhibits safe operation and distinct noise characteristics in its healthy operational state, primarily attributed to the dominant single-tone noise of the Blade Passage Frequency (BPF) and its harmonics, along with broadband noise resulting from random turbulent pulsations (Maaloum *et al.*, 2004; Polacsek *et al.*, 2006). However, the stability of the flow field within its internal blade channel is significantly disrupted due to unsteady disturbances when the maritime compressor operates outside its design conditions, such as in the presence of rotating stall. This disruption leads to a considerable deterioration in the marine compressor's aerodynamic performance and may even result in major safety incidents (Zhao *et al.*, 2023). Moreover, the internal blade flow channel of the compressor during rotating stall experiences phenomena such as backflow and substantial air flow separation, giving rise to distinct aerodynamic noise characteristics that deviate from those observed under design working conditions (Kameier and Neise, 1997). Consequently, conducting an in-depth investigation into the flow and noise characteristics of marine compressors prior to the occurrence of rotating stall becomes imperative as a prerequisite for the development of early warning detection technology for unstable operating conditions, including compressor rotating stall and surge, with a distinct focus on applications within the sphere of ship and ocean engineering.

Particular attention had been given by researchers to the underlying cause of rotational stall in the investigation of the flow field during compressor stall, known as rotating instability. rotating instability represented an unsteady phenomenon occurring within the rotor domain before compressor stalling and fell under the category of flow disturbances preceding stall (Day and Asme, 2015). Baumgartner et al. (Baumgartner *et al.*, 1995) discovered that the vibration frequency induced by aerodynamic forces did not resonate with the rotor speed harmonic, leading them to propose rotating instability for the first time through a comparison of pressure pulsation and vibration data from the first stage rotor tip region of a multistage compressor. Subsequent simulations conducted by Vo et al. (Vo, 2010) on an isolated rotor demonstrated that rotating instability likely resulted from the reflux phenomenon occurring at the back of the blade tip gap. Similarly, Marz et al. (Marz *et al.*, 2002) undertook a more comprehensive analysis of the physical mechanisms behind rotating instability, employing experimental and numerical approaches. A vortex structure was discovered forming in the leading-edge plane of the blade, resulting from the combined effects of tip gap flow, axial reverse flow, and incoming flow. The formation and progression of this vortex structure were identified as the primary cause of instability. Additionally, Mailach et al. (Mailach *et al.*, 2001) utilized laser-doppler-anemometry to measure the unsteady pressure distribution in the blade channel and tip gap. The findings revealed that rotating instability was, in fact, attributable to the generation of a rotating structure with high mode orders, arising from the periodic interaction between the tip vortex and adjacent blades. Pullan et al. (Pullan *et al.*, 2015) presented the path of vortex structure propagation within the spike-type rotating stall, which stemmed from the pressure loss in the rotor tip region resulting from flow separation induced at high incidence drawing on numerical simulations. Recent studies on rotating instability have primarily focused on techniques for stall suppression. Tomita et al. (Tomita and Furukawa, 2020) examined the impact of tip leakage vortex breakdown on internal flow. The results demonstrated that the stall phenomenon in centrifugal compressors was mainly driven by the tip leakage flow, and controlling this flow represented an effective means to enhance the operational range of the compressor. Furthermore, Brandstetter et al. (Brandstetter *et al.*, 2019) experimentally observed the feedback mechanism between the acoustic resonance of a transonic fan and the aeroelastic disturbances, thereby proposing the possibility of complex multiphysics coupling in the modal oscillation preceding stall for the first time.

Indeed, rotating instability was accompanied by a distinct acoustic spectral characteristic, characterized by a narrowband amplitude peak that differs from the BPF and its harmonics. Kameier et al. (Kameier and Neise, 1997) conducted the first comprehensive experimental investigation into the noise characteristics of mechanical rotating instability in axial turbomachinery following Baumgartner's formal proposition of the rotating instability concept. Pronounced peaks in a narrow frequency band below the BPF were observed. Measurement results indicated that the tip gap noise was associated with flow instability caused by reverse flow within the tip gap. Subsequently, Cudina (Cudina, 2001) conducted a detailed examination of the noise spectrum of axial fans equipped with inlet guide vanes under adjacent stall conditions. Fukano and Jang (Fukano and Jang, 2004), as well as Pardowitz et al. (Pardowitz *et al.*, 2014; Pardowitz *et al.*, 2015), explored the velocity pulsation characteristics and rotating instability of turbomachinery through experimental approaches, thereby proposing the fundamental mechanism behind the peak frequency observed in vortical flow under rotating instability.

Simultaneously, the advancement of Computational Fluid Dynamics (CFD) has facilitated the use of numerical simulations as an efficient approach to investigating noise characteristics under unstable operating conditions. A comprehensive numerical simulation of a centrifugal compressor under near-surge conditions was conducted by

Galindo et al. (Galindo *et al.*, 2015) utilizing the detached eddy simulation turbulence model. The results revealed that while the reduction of the tip gap significantly impacted the compressor's aerodynamic performance, it did not exhibit a significant effect on noise performance. Zhu et al. (Zhu and Carolus, 2018; Zhu *et al.*, 2018) employed the Lattice Boltzmann Method to thoroughly study the generation mechanism of narrowband noise under the rotational stall, accompanied by pressure field decomposition. Dehner et al. (Dehner *et al.*, 2022) performed pressure field decomposition on the induced plane of the turbocharger. The results demonstrated that as the supercharger transitioned to a stall condition with reduced flow, the mode content of the compressor shifted towards higher-mode numbers and frequencies, consequently leading to the occurrence of the whoosh noise during the stall.

Nevertheless, the utilization of Aeroacoustic methods for the prediction and assessment of aerodynamic noise in rotating machinery remains a formidable challenge. Since the inception of the field of aeroacoustics by Lighthill (Lighthill, 1952) in 1954, and the formulation of the free field prediction formula for aerodynamic noise of rotating machinery by Ffowcs Williams and Hawkings (Williams and Hawkings, 1969) in 1969, the Finite Element Method (FEM) has become a widely adopted approach for conducting aerodynamic noise of rotating machinery within intricate spatial configurations. In recent years, a multitude of scholars in Europe and Canada have contributed valuable insights into methods for assessing aerodynamic noise in rotating machinery(Casalino *et al.*, 2019; Ianniello, 2020; Casalino *et al.*, 2021; Kholodov and Moreau, 2021; Sanjose *et al.*, 2021). Building upon this foundation, some scholars have subsequently advanced the application of FEM methods in the domain of aerodynamic noise (Kraxberger *et al.*, 2023; Schoder, 2023b; a; Schoder and Wurzinger, 2023). OpenCFS, an open-source framework for solving partial differential equations with finite elements, was introduced by Schoder et al. (Schoder and Roppert, 2022; Schoder, 2023c; Schoder and Roppert, 2023) Additionally, CFS-Data, the pre-processing component of OpenCFS, which incorporates random noise sound fields and radiation models, was also provided. Moreover, human vowel production was simulated by Lasota et al. (Lasota *et al.*, 2023) using the Openfoam and OpenCFS open-source frameworks. The outcomes indicated that the pronunciation model predicted by the new subgrid-scale anisotropic minimum dissipation is more akin to natural speech than conventional subgrid-scale models. The aeroacoustics workflow of the perturbed convective wave equation and the Ffowcs Williams and Hawkings analogy was tested by Schoder et al. (Schoder *et al.*, 2020), concentrating on the convergence issues of CFD and computational acoustic meshes. Ultimately, the results obtained from the perturbed convective wave equation and Ffowcs Williams-Hawkings (FW-H) predictions were essentially identical.

Considerable progress has been made in investigating the noise associated with rotating instability, yielding valuable results (Pardowitz *et al.*, 2015; Zhu and Carolus, 2018). However, there is a scarcity of studies focusing on the noise generated during compressor stall, particularly concerning 1.5-stage axial compressors (Broatch *et al.*, 2015; Galindo *et al.*, 2015). The intricate nature of 1.5-stage axial compressors, encompassing three blade rows (namely, the guide vane, rotor, and stator), results in multiple noise sources and an escalation in computational expenses for simulations. Moreover, a more comprehensive analysis and research on the intricate flow structure responsible for generating aerodynamic noise sources during stall in 1.5-stage axial compressors remains lacking. Consequently, it becomes imperative to characterize the noise characteristics of these axial compressors under unstable operating conditions, with the ultimate aim of extending the application to multi-stage axial compressors.

In this paper, the Shear Stress Transport turbulence model is employed to obtain the steady and unsteady flow characteristics of the marine compressor at the highest efficiency point and the near-stall point. Detailed analysis is conducted to explore the disparities in the flow structure between the highest efficiency and near-stall points, revealing the presence of additional peak frequencies and complex flows that serve as newly identified noise sources under near-stall conditions. The intensities of these noise sources and the corresponding free-field sound power levels are examined to investigate the compressor's noise characteristics near the stall. Additionally, the acoustic response within the actual duct is investigated to provide insights into the noise conditions when the compressor operates in proximity to the stall on an actual test bench.

II. SIMULATION STRATEGIES

A. Description of the marine 1.5-stage axial compressor

Figure 1 presents the numerical calculation domains of the 1.5-stage axial compressor used for marine gas turbines, encompassing three blade rows: the guide vane, rotor, and stator. Appropriate extensions are applied to the inlet and outlet regions to ensure a stable flow. It is worth noting that the compressor test bench includes a horn-shaped inlet and an exhaust volute, with the latter serving as a compromise component for accommodating the motor and gearbox alignment in a coaxial configuration. They are excluded from the calculation domains to minimize computational expenses as the horn-shaped inlet and exhaust volute do not actively participate in the gas compression process but solely serve to direct the airflow. The remaining parameters pertinent to the 1.5-stage axial compressor are displayed in Table I.

B. CFD mesh and boundary conditions

A fully hexahedral structured mesh is employed in this study to mitigate errors arising from mesh orthogonality. The domain of the guide vane is extended upstream from the leading edge by 2 times the guide vane chord length, while the stator domain is extended downstream from the trailing edge by 1.5 times the stator chord length to ensure complete flow development. These extension distances have been previously utilized in studies to yield favorable results (Li *et al.*, 2021). It plays a crucial role in the aerodynamic performance and noise characteristics of the compressor despite there being a small tip clearance of the rotor in this paper, which is 0.5 mm. Previous investigations have extensively examined the tip gap, encompassing its aerodynamic properties (Du *et al.*, 2008; Zhang *et al.*, 2021) and noise characteristics (Boulamatsis *et al.*, 2019; Avallone *et al.*, 2020). Notably, the formation of the tip leakage vortex associated with the blade tip gap under adjacent stall conditions constitutes the primary source of aerodynamic noise characteristics (Karstadt *et al.*, 2010; Moghadam *et al.*, 2019), emphasizing the significance of considering the tip leakage vortex in this study. The gap sizes below 2 mm necessitate a minimum of 15 layers of prism nodes based on previous research (Wei *et al.*, 2018a; Wei *et al.*, 2018b; Wang *et al.*, 2020). A total of 20 prism layers are implemented to accurately capture the flow within the 0.5 mm tip clearance in this paper.

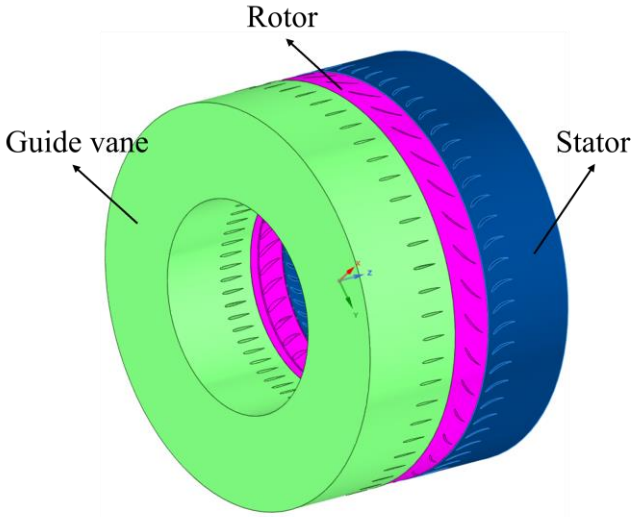

Figure 1. The configuration of the 1.5-stage axial compressor model.

Table I. Geometry specification for the 1.5-stage axial compressor.

Parameter	Guide vane	Rotor	Stator
Maximum diameter /mm	458.4	458.4	458.4
Hub-to-tip ratio	0.53	0.53	0.57
Blade height /mm	107.4	107.4	96.1
Mid chord /mm	30	36	36
Aspect ratio	3.58	2.88	2.67
Number of blades	54	37	60
Solidity at mid span	0.74	0.60	0.96
Tip clearance size /mm		0.5(1.4% chord)	

Rotating speed /r/min	2270

Primary consideration should be given to the shear stress transport turbulence model, which represents a low Reynolds number model within the Reynolds average turbulence model framework as per numerous prior numerical simulation investigations on turbomachinery (Yang and Wu, 2014; Shi *et al.*, 2019). The compressor full-channel mesh details are depicted in Figure 2, featuring 13 boundary layers on all walls to effectively simulate the velocity gradient and separated flow near the wall. It ensures that the distribution of viscous effects is directly resolved by mesh nodes, without relying on approximate wall functions. In essence, the shear stress transport turbulence model imposes stringent requirements on the wall-adjacent mesh, necessitating a y+ value of less than 5 in the core region (Anand *et al.*, 2018; Sajadmanesh *et al.*, 2019) to accurately capture the flow behavior near the wall. The y+ distribution on the blade surfaces at the highest efficiency point is shown in Figure 3, where the maximum y+ value does not exceed 3.5, indicating an acceptable level of fidelity. Owing to the favorable flow conditions at the highest efficiency point, where the flow speed is significantly higher than that of near-stall point. It can be inferred that the y+ near the stall point must also satisfy the prerequisites for CFD calculations, given that the y+ at the highest efficiency point meets the requirements of the turbulence model, as the identical set of CFD grid is employed in both operational conditions.

It is necessary to perform grid independence verification to guarantee the insensitivity of the calculation results to the number of cells. In this study, Richardson extrapolation is applied to assess the discretization error of the grid (Schoder *et al.*, 2021). Extrapolated values, representing estimates at infinite grid density, were computed using three distinct sets of grids. Detailed information regarding the grids is presented in Table II. In this context, N1, N2, and N3 respectively denote the number of cells in the three sets of grids, and $\phi_{Total\_pressurei}(i=1,2,3)$ represents the total pressure value calculated by the i-th grid. In accordance with literature requirements (Celik *et al.*, 2008), the density among different grids must adhere to criterion $r_{i,j}=\frac{h_i}{h_j}>1.3$, with specific attention given to parameter $h=\left[\frac{1}{N}\sum_{i=1}^{N}(\Delta V_i)\right]^{1/3}$, Here, ΔV_i represents the volume of grid cells, and N denotes the total number of cells employed for the computations. As a consequence of this analysis, extrapolations are performed to estimate the values of $\phi_{\mathrm{ext}}^{32}=1125\,\mathrm{Pa}$ and $p=1.78$. By employing the definition of Grid Convergence Index (GCI) found in the literature, the ultimate uncertainty $\mathrm{GCI}_{fine}^{32}=3.6\%$ is derived. This indicates that the numerical uncertainty of the total pressure on the fine grid is 3.6%. Three sets of distinct meshes are employed to evaluate the variation in the calculation results in this study, as illustrated in Figure 4. The disparity between the experimental and simulated results diminishes with the decrease in the normal cell size estimate h, and the discrepancy among the third grid and extrapolated value sets becomes practically negligible. Consequently, the third grid yield matched results with beneficial convergence properties. Concerning the specific implementation plan for acquiring experimental data in the figure, reference is encouraged to be made to previous research. (Lu *et al.*, 2022; Lu *et al.*, 2023)

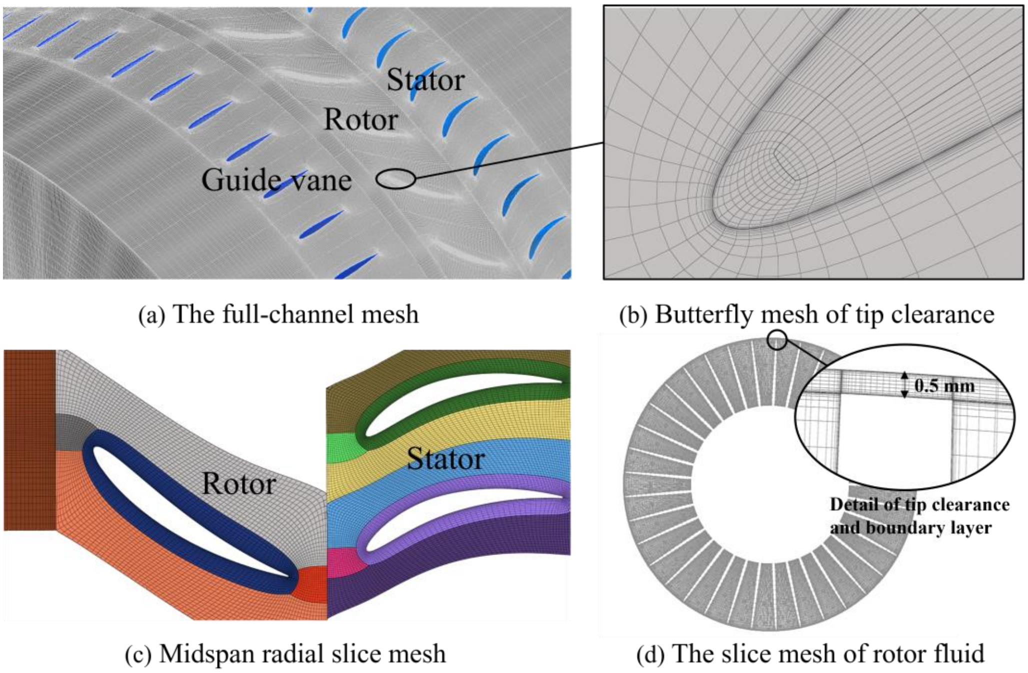

Figure 2. CFD mesh of the 1.5-stage axial compressor.

Table II. Sample calculations of discretization error.

	$\phi_{Total\_pressure}$
N1, N2, N3/million	14, 19, 27

r_{21}	1.52
r_{32}	1.47
$\phi_{Total\_pressure1}$/Pa	1093
$\phi_{Total\_pressure2}$/Pa	1104
$\phi_{Total\_pressure3}$/Pa	1116

The CFD calculations are performed using the CFX code, which is based on the aforementioned fully structured mesh. The simulation settings are summarized in Table III. High-order spatial discretization is employed, and the tangential velocity of all walls is specified as no-slip. Adiabatic heat exchange mode is assumed. The rotor operates at a speed of 2270 r/min, and the inlet is assigned a total pressure of 101325 Pa and a total temperature of 288.15 K, while the outlet has a specified radial average static pressure. In particular, subsequent to the computation of the characteristic curve, the outlet pressure at the point of highest efficiency is determined to be 101750 Pa, whereas the outlet pressure proximate to the stall condition is found to be 102012.5 Pa. The rotor region is modeled as rotating using the Multiple Reference Frame approach in the steady simulation, while the remaining regions are treated as stationary. The rotor-stator interface utilizes the Mixing-Plane model for the exchange of upstream and downstream data. The unsteady scheme initializes with the results from the steady calculation to expedite convergence, and the transient flow at the rotor-stator interface is captured using the Transient Rotor Stator method. The time step in this study is set to 1.78593 × 10-5 s, corresponding to a rotation of 0.24 degrees per time step, with a total of 40-time steps required for one rotor channel. This temporal resolution is significantly higher compared to previous works by other researchers (Polacsek *et al.*, 2006; Hu *et al.*, 2013; Zhang *et al.*, 2016), where a rotor channel had only 20-time steps and a rotation of 1 degree corresponded to the one-time step.

Table III. The numerical simulation settings.

Condition	Steady	Unsteady
Inlet	Pressure-inlet	Pressure-inlet
Outlet	Pressure-outlet	Pressure-outlet
Spatial discretization resolution	High-order	High-order
Temporal schemes	Auto Timescale	Implicit
Wall tangential velocity	No-slip	No-slip
Heat exchange mode	Adiabatic	Adiabatic
Rotation model	Multiple Reference Frame	Sliding mesh

The Mach number in the rotor's tip region has reached 0.4 despite the relatively low-pressure ratio of the studied 1.5-stage compressor, rendering the incompressible assumption inadequate. The incompressible hypothesis tends to overlook flow and density fluctuations arising from rotor rotation in aerodynamic noise investigations, which contribute to the mass source in the aerodynamic noise generation. Consequently, a compressible flow model is adopted, necessitating the inclusion of the energy equation in the solution procedure.

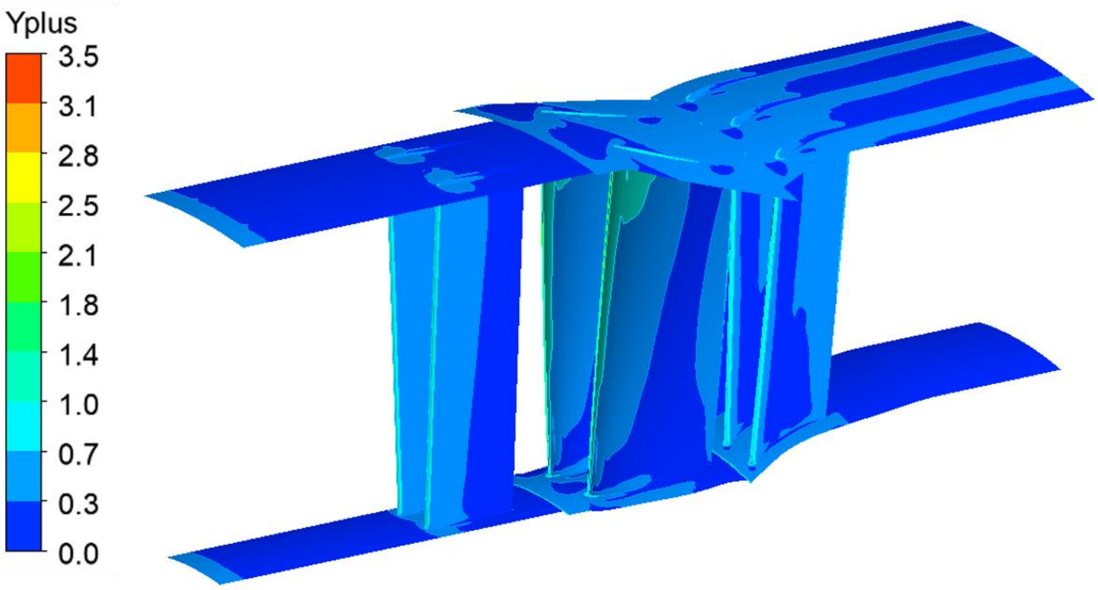

Figure 3. The y+ distribution on the blade surfaces.

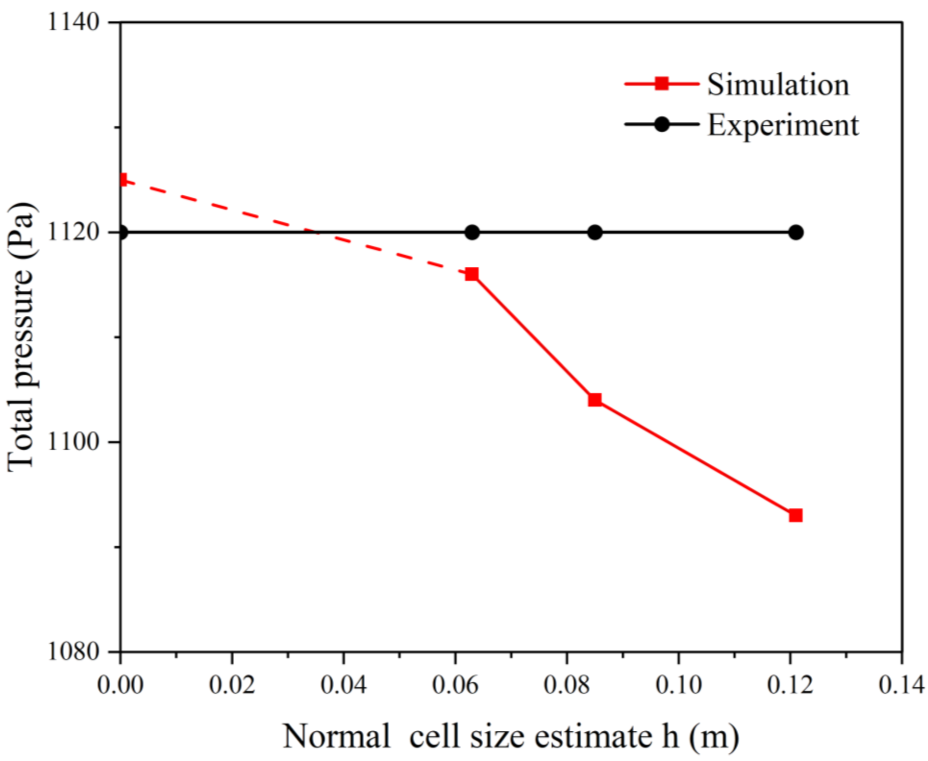

Figure 4. Grid convergence regarding mesh refinement using Richardson extrapolation.

C. Governing equations and turbulence model

The continuity, mass, and energy equations within the Navier-Stokes equation framework are given by

$$\frac{\partial \rho}{\partial t} + \nabla \cdot (\rho \bar{\mathbf{v}}) = 0, \tag{1}$$

$$\frac{\partial}{\partial t}(\rho \bar{\mathbf{v}}) + \nabla \cdot (\rho \bar{\mathbf{v}} \otimes \bar{\mathbf{v}}) = -\nabla \cdot \bar{p}\mathbf{I} + \nabla \cdot \left(\bar{\mathbf{T}} + \mathbf{T}_{RANS}\right) + \mathbf{f}_b, \tag{2}$$

$$\frac{\partial}{\partial t}(\rho \bar{E}) + \nabla \cdot (\rho \bar{E} \bar{\mathbf{v}}) = -\nabla \cdot \bar{p}\bar{\mathbf{v}} + \nabla \cdot \left(\bar{\mathbf{T}} + \mathbf{T}_{RANS}\right)\bar{\mathbf{v}} - \nabla \cdot \bar{\mathbf{q}} + \mathbf{f}_b \bar{\mathbf{v}}. \tag{3}$$

where $\bar{\mathbf{v}}$ represents the time-averaged velocity, ρ is the density, $\bar{p}$ is the time-averaged pressure, $\mathbf{I}$ is the unit tensor, $\overline{\mathbf{T}}$ is the time-averaged viscous stress tensor, $\mathbf{f}_b$ is the resultant force of body forces (such as gravity and centrifugal force), $\bar{E}$ is time-averaged total energy per unit mass and $\overline{\mathbf{q}}$ average heat flux. The presence of the stress tensor $\mathbf{T}_{RANS}$ can be written as

$$\mathbf{T}_{\mathrm{RANS}} = -\rho \begin{pmatrix} \overline{u'u'} & \overline{u'v'} & \overline{u'w'} \\ \overline{u'v'} & \overline{v'v'} & \overline{v'w'} \\ \overline{u'w'} & \overline{v'w'} & \overline{w'w'} \end{pmatrix} + \frac{2}{3}\rho k\mathbf{I}. \tag{4}$$

In this work, the shear stress transport turbulence model (Menter, 1994) is used to close the governing equations. Previous studies have shown that the tonal noise of rotating machinery can be accurately predicted using this model.

The transport equations for k and ω are

$$\frac{\partial}{\partial t}(\rho k) + \nabla \cdot (\rho k \overline{\mathbf{v}}) = \nabla \cdot \left[\left(\mu + \sigma_k \mu_t \right) \nabla k \right] + P_k - \rho \beta^* \omega k, \tag{5}$$

and

$$\begin{aligned} &\frac{\partial}{\partial t}(\rho \omega) + \nabla \cdot (\rho \omega \overline{\mathbf{v}}) = \nabla \cdot \left[\left(\left(\mu + \sigma_\omega \mu_t \right) \nabla \omega \right] \\ &+2\left(1 - F_1\right) \frac{\rho \sigma_{\omega 2}}{\omega} \nabla \cdot (k) \nabla \cdot (\omega) + \frac{\gamma}{v_t} P - \beta \rho \omega^2. \end{aligned} \tag{6}$$

In the Eq. (5) and Eq. (6),

$$P_k = \min\left(P, 10\beta^* \rho k \omega\right), \tag{7}$$

$$\mu_t = \frac{\rho a_1 k}{\max\left(a_1\omega, SF_2\right)}, \tag{8}$$

$$\gamma = \frac{\beta}{\beta^*} - \frac{\sigma_{\omega 2} k^2}{\sqrt{\beta^*}}, \tag{9}$$

$$S = \sqrt{2S_{ij}S_{ij}}, \tag{10}$$

$$S_{ij} = \frac{1}{2}\left(\frac{\partial u_i}{\partial x_j} - \frac{\partial u_j}{\partial x_i}\right). \tag{11}$$

where p represents the turbulent kinetic energy generation term, F_1 is the hybrid function, S_{ij} is the strain rate tensor. β^*, a_1, β, $\sigma_{\omega 2}$, σ_k are the model constants.

D. The weak variational form of Lighthill's theory

The variational form of the Lighthill equation is used for compressor noise prediction. The Lighthill equation is given by (Lighthill, 1952)

$$\frac{\partial^2 \rho_a}{\partial t^2} - a_0^2 \frac{\partial^2 \rho_a}{\partial x_i \partial x_i} = \frac{\partial^2 T_{ij}}{\partial x_i \partial x_j}. \tag{12}$$

where a_0 is the speed of sound, ρ_a is the density pulsation, and T_{ij} is the Lighthill stress tensor. After frequency domain transformation this becomes

$$-\omega^2 \rho_a - a_0^2 \frac{\partial^2 \rho_a}{\partial x_i \partial x_i} = \frac{\partial^2 T_{ij}}{\partial x_i \partial x_j}. \tag{13}$$

Introducing the potential function ψ and applying the weighted residual method variation gives

$$\frac{\omega^2}{a_0^2}\psi+\frac{\partial^2\psi}{\partial x_i \partial x_i}=\frac{1}{i\omega}\frac{\partial^2 T_{ij}}{\partial x_i \partial x_j}. \tag{14}$$

The weak variational form associated with Equation (14) can be written as

$$\begin{aligned}&-\int_\Omega \frac{\omega^2}{\rho_0 a_0^2}\psi\delta\psi d\Omega-\int_\Omega \frac{1}{\rho_0}\frac{\partial\psi}{\partial x_i}\frac{\partial\delta\psi}{\partial x_i}d\Omega\\&=\int_\Omega \frac{i}{\rho_0\omega}\frac{\partial\delta\psi}{\partial x_i}\frac{\partial T_{ij}}{\partial x_j}d\Omega-\int_\Gamma \frac{\delta\psi}{i\rho_0\omega}\frac{\partial}{\partial x_i}\left(a_0^2\rho_a\delta_{ij}+T_{ij}\right)n_i d\Gamma.\end{aligned} \tag{15}$$

The right two items of Equation (15) represent the contribution of volume and surface noise sources, respectively. Further detail on the variational form of Lighthill's analogy is given by Oberai et al. (Oberai *et al.*, 2000; 2002).

The acoustic code utilized in manuscript is ACTRAN. With respect to discretization, in the inner domain Ω_i, the variable y is locally interpolated on each finite element using a set of interpolation functions $N_i(\xi)$ defined in terms of local coordinates ξ:

$$\psi(\xi)=\sum_{i=1}^{N}N_i(\xi)\psi_i. \tag{16}$$

The selection of a Galerkin approach (test and trial functions are extracted from the same functional space) leads to the following algebraic system:

$$\left(-\mathbf{K}+\omega^2\mathbf{M}\right)\Psi=\mathbf{F}^{aero}. \tag{17}$$

where matrices K and M result from the assembly of the related element matrices:

$$\begin{aligned}\mathbf{K}&=\sum_e \mathbf{K}^e,\\ \mathbf{M}&=\sum_e \mathbf{M}^e.\end{aligned} \tag{18}$$

and the right-hand side vector F is obtained by assembling contributions in the right hand side involving aerodynamic sources computed using CFD results fields $\mathbf{F}^{aero}$ is the volume integral which correspond to the aerodynamic noise excitation.

E. Noise prediction scheme

An aerodynamic noise prediction approach is employed, which utilizes a hybrid method in this paper. Initially, Lighthill's variational theory is employed to extract aerodynamic noise sources from the flow fields. Subsequently, the FEM is employed to conduct noise propagation calculations. Hybrid methods that combine CFD with computational aeroacoustics have gained popularity in this regard. These methods involve separate calculations of the flow field and sound field. Firstly, unsteady flow field computations are conducted to determine the aerodynamic noise sources. Then, the far-field acoustic radiation is predicted based on the noise sources obtained from the CFD computations.

In practical applications, sound prediction under complex structures can be effectively achieved using the FEM, which allows for comprehensive modeling and analysis of sound reflection and scattering. The combination of the Lighthill acoustic analogy with the variational form presents inherent advantages over the integral form of the Boundary Elements Method (BEM) when dealing with complex structures and low-frequency noise propagation (Ren *et al.*, 2022). The effectiveness of this simulation approach has been assessed by various scholars in the context of air-conditioning systems (Kierkegaard *et al.*, 2016), axial compressors (Lu *et al.*, 2022), and centrifugal compressors (Ren *et al.*, 2022). The evaluation results demonstrate the high accuracy of the aforementioned strategy for predicting interior aerodynamic noise in turbomachinery. Specifically, the integration interpolation technique is utilized to map the velocity and density data from the fluid mesh to the acoustic mesh, which ensures maximal retention of information from CFD grid interpolation to the acoustic mesh, after which the data from each region are converted into contributions from the volume and surface noise sources. A flowchart depicting the prediction process based on CFD results is presented in Figure 5.

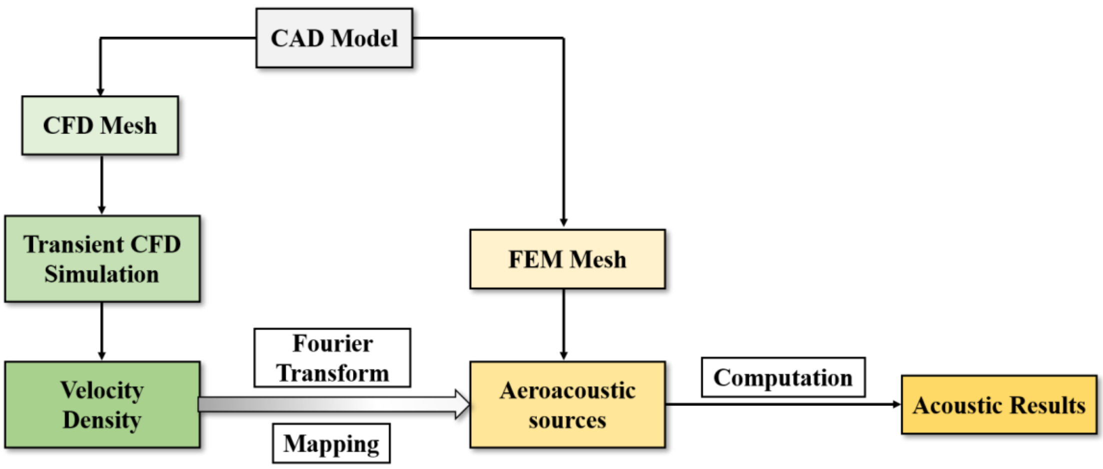

Figure 5. The flowchart of the prediction process based on CFD results.

For turbomachinery applications, the dominant noise is typically attributed to the single-tone component associated with the BPF (Polacsek *et al.*, 2006), necessitating the consideration of the first three harmonics of the BPF. The BPF and its corresponding harmonic frequencies are determined by Equation (19)

$$f = \frac{nBi}{60}. \tag{19}$$

where n is the rotor speed, B is the number of rotor blades, i is the harmonic order, and f is the blade passing frequency. In the case of the compressor under investigation, the third-order BPF corresponds to a frequency of 4200 Hz. To ensure appropriate analysis, the maximum frequency of interest for this study was set at 5000 Hz.

Numerous studies have explored the required size of the acoustic mesh for noise calculations (Hu *et al.*, 2013; Zhang *et al.*, 2016). These studies have demonstrated the necessity of maintaining at least six elements within the wavelength of the highest frequency noise. The acoustic mesh encompassed eight elements within the wavelength of the highest frequency noise in this research, resulting in a total of 12 million cells, as depicted in Figure 6.

It is important to note that although the exhaust volute does not directly participate in the gas compression process, its impact on noise transmission cannot be disregarded. This complex structure significantly affects noise propagation due to the absence of anechoic treatment in the exhaust volute area of the actual test bench, as confirmed in previous investigations (Lu *et al.*, 2022). The outlet acoustic boundary of the volute was designed to emulate free duct modes, simulating an infinitely long rectangular duct. This configuration ensures that acoustic modes within the frequency range of 5000 Hz pass through the rectangular section without experiencing reflections. Furthermore, the flow tube was fully modeled, accounting for the 16mm thick wall, and the inlet area was configured as a semi-open free space. The circular-like boundary of the inlet area serves as a non-reflective surface, enabling the inlet to exhibit characteristics akin to open space.

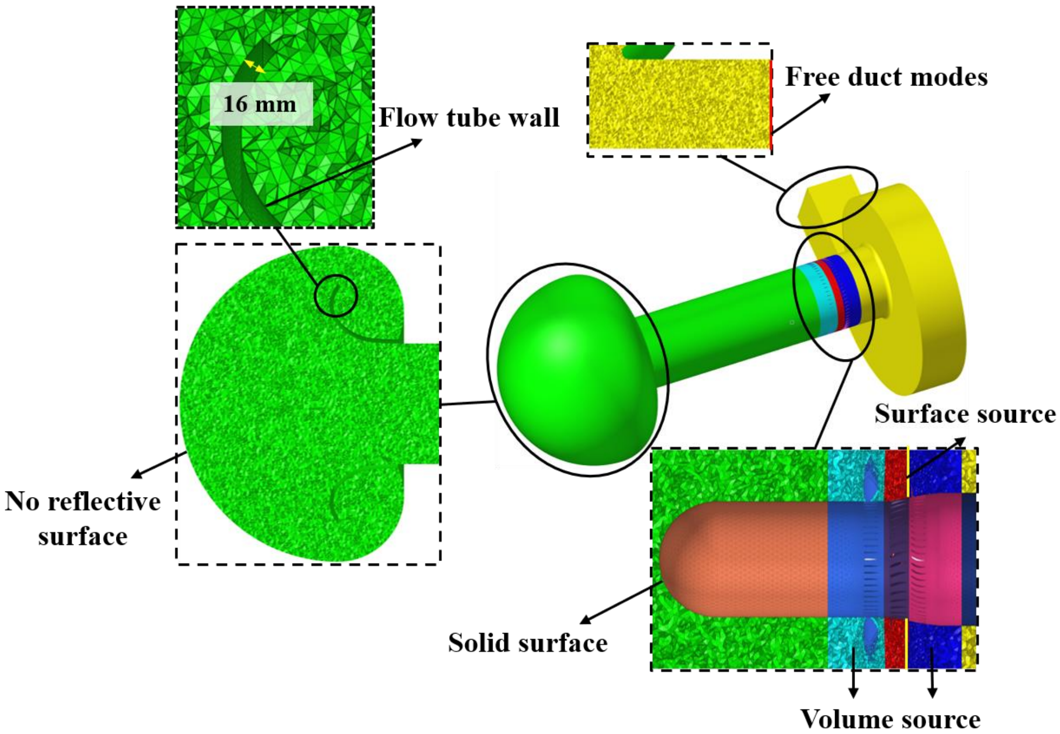

Figure 6. Acoustic mesh for CAA mode of the 1.5-stage compressor.

III. RESULTS AND DISCUSSION

A. Validation of simulation scheme

The experimental investigation detailed in this article was conducted on a compressor test bench. Within the suction part of the test bench, a flow tube featuring a horn-shaped inlet was employed to stabilize airflow and facilitate mass flow measurements. In the exhaust system, an exhaust volute and a throttle valve were incorporated to ensure compliance with the experiment's exhaust pressure requirements. A DC frequency modulation motor, connected to a variable speed gearbox, was utilized to drive the compressor.

Flow field measurements comprised both steady-state and dynamic measurement systems. The schematic representation of the steady-state measurement system, as depicted in Figure 7, served to assess the overall aerodynamic performance of the compressor. This characterization encompassed measurements of total pressure, total temperature, and mass flow. In section A, four static pressure probes were arranged circumferentially, forming a flow measurement system in conjunction with the surrounding environment. For mutual validation of measurement results from section A, a gas mass flow meter was installed in section B. Section C featured two three-hole comb probes and two total temperature probes, measuring total pressure and total temperature before the front support. Additionally, three-hole comb probes were positioned in sections D, E, and F to measure the total pressure at the inlet, interstage, and outlet, respectively. The total temperature of the outlet was ascertained using the total temperature probe in section G.

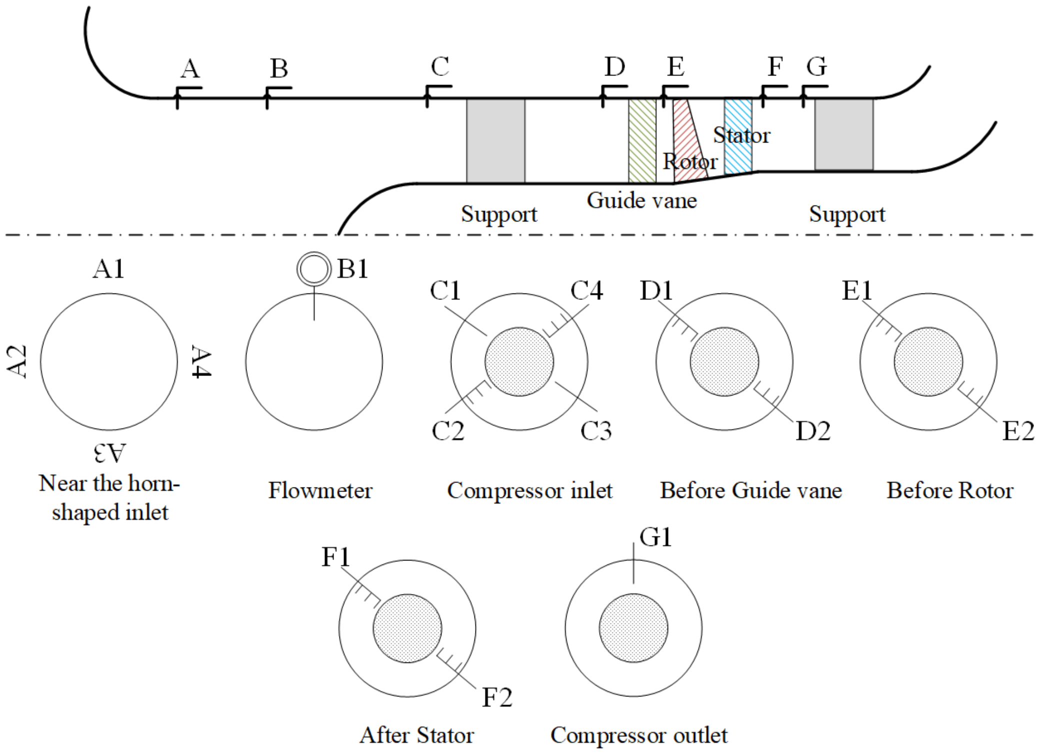

Figure 7. Compressor aerodynamic performance measurement location.

A test bench is established at Harbin Engineering University to validate the accuracy of the numerical calculations, as illustrated in Figure 8. The compressor's performance is assessed by conducting measurements of various thermodynamic parameters while maintaining a fixed throttle opening and rotor speed. The parameters of interest encompass the total pressure, total temperature, and mass flow, which facilitate the comprehensive evaluation of the compressor's characteristics. The overall behavior of the compressor is quantified employing the total pressure ratio, denoted as π, and the efficiency, denoted as Eff. These performance indicators can be mathematically defined as follows:

$$\pi = \frac{P_{out}}{P_{in}}, \tag{20}$$

$$Eff = \frac{\pi^{\frac{k-1}{k}} - 1}{T_{out} / T_{in} - 1}. \tag{21}$$

where P_{out} and P_{in} are the total pressure of the outlet and the inlet, respectively, and k is the specific heat ratio of air. T_{out} and T_{in} are the outlet and inlet total temperatures, respectively.

The focus of this paper lies in examining the flow and noise characteristics of the compressor at the highest efficiency and near-stall operating points. The position of these two points on the performance curves, specifically the curves of total pressure ratio and efficiency, is depicted in Figure 9. This depiction is achieved by manipulating the radial average static pressure at the outlet. As the outlet pressure increases, the compressor's mass flow gradually diminishes, while the pressure ratio and efficiency initially rise before declining. As the exhaust pressure further escalates, the flow within the compressor becomes more constrained, with the blade channel experiencing gradual blockage until the compressor enters the stall condition. Moreover, a comparison between the overall compressor characteristics obtained from the flow field calculations and experimental results demonstrates a satisfactory level of agreement, thereby affirming the reliability of the CFD results. The actual disparity between the two curves remains within 0.002, although the figure may present a notable difference between the experimental and simulated total pressure ratios, primarily due to the enhanced resolution of the left vertical axis.

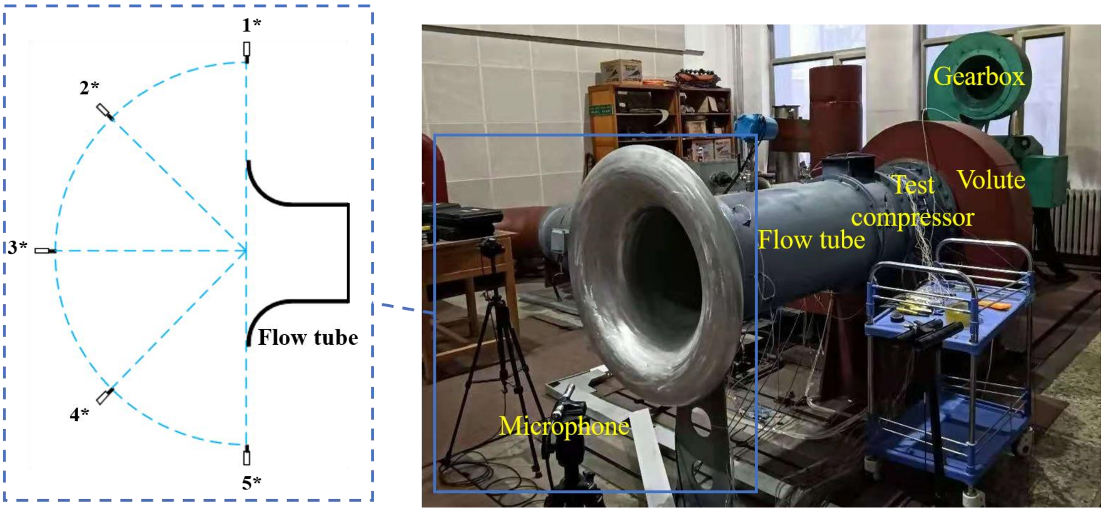

Figure 8. The arrangement of the compressor test bench.

The B&K test system is employed to measure noise in the 1.5-stage compressor in terms of noise measurement. The noise signal is captured by the microphones, transmitted to the data exchange, and then connected to a laptop for storage as digital data for subsequent analysis. B&K 4957 microphones are utilized as acoustic sensors in the experiment. They are positioned 1 meter away from the center of the inlet plane, with an angular separation of 45 degrees, as illustrated in Figure 8. Owing to constrained experimental conditions, there are no solid walls within a 6-meter radius of the inlet area, except for the ground to mitigate the undesirable effects of other obstacles on the noise measurement results. Additionally, all walls beyond 6 meters are covered with anechoic material to effectively absorb the propagated sound waves. Nevertheless, certain errors in the experimentally measured data are inevitably induced by the acoustic measurement environment, as illustrated in Figure 10. The measurement duration for each working condition is set to 35 seconds to ensure adequate noise resolution.

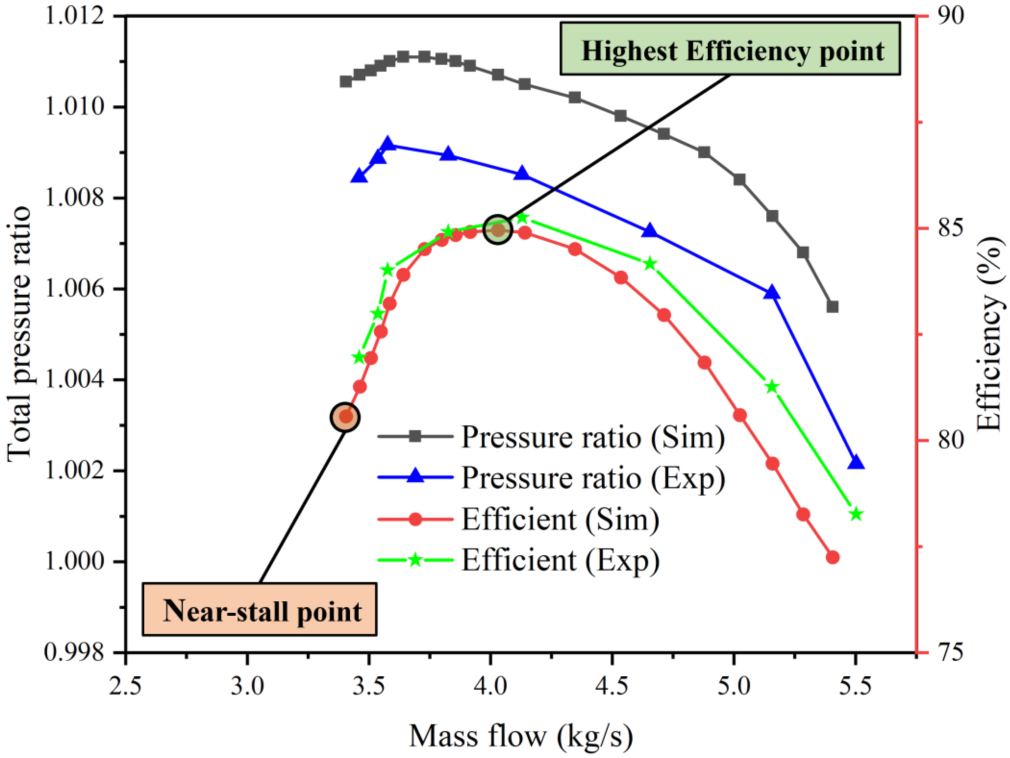

Figure 9. Validation of simulation accuracy and selection of operating points.

A detailed comparison has been conducted to analyze the noise results in the previous work (Lu *et al.*, 2022), with the double validation involving instantaneous quantities and noise. The results of the previous study are referenced to validate the accuracy of the noise prediction results in this paper, as depicted in Figure 10. It is widely recognized that discrete noise plays a prominent role in turbomachinery aeroacoustics and significantly influences the Sound Pressure Level (SPL). The agreement between the simulated and experimentally measured discrete noise at monitoring point 2 indicates a close match, thus affirming the accuracy of the simulation. Furthermore, the simulated total SPL at five measurement points near the inlet also exhibits favorable agreement with the experimental data, with a minimal error of approximately 1 dB. However, a larger discrepancy of about 5 dB is observed at measurement point 4. This issue is attributable to several factors. Firstly, challenges arise from the acoustic measurement environment, where ensuring a completely free field at the compressor inlet proves difficult. Secondly, unlike a fan, the compressor needs numerous auxiliary equipment. However, a compressor test bench encompasses various auxiliary components, including high-power motors, matching gearboxes, lubricating oil supply systems, etc. The initiation of these auxiliary components is a prerequisite for starting the compressor, ensuring its safe operation. The presence of numerous auxiliary components inevitably introduces complexities affecting experimental measurements. Ultimately, the compressor itself is characterized by significant size and the multitude of blades. Undertaking a comprehensive refined CFD calculation on the compressor proves to be an exceptionally challenging endeavor due to the immense computing resources it demands. In the realm of aerodynamic noise, the performance of detached eddy simulation or large eddy simulation on compressors is challenging.

Resorting solely to the Reynolds-averaged turbulence model becomes the only viable option for evaluating compressor aerodynamic noise. Within this context, achieving an accurate capture of the aerodynamic noise sources of the compressor poses a formidable challenge.

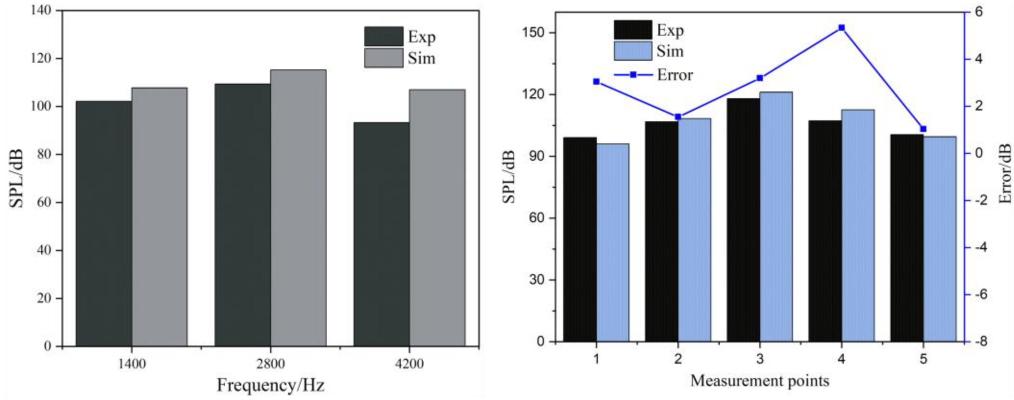

(a) The SPL at point 2 at the BPF and its harmonics. (b) Simulation and experimental comparison of SPL

Figure 10. Validation of noise prediction of measurement points.

B. Steady flow characteristics

The steady flow characteristics of the simulation are initially examined to compare the flow characteristics at the highest efficiency point and the near-stall point. Figure 11 presents the static entropy distribution of both points in order to highlight the differences between the highest efficiency point and the near-stall point more clearly. The complete stall point is obtained by increasing the outlet pressure from the near-stall point shown in Figure 9, which corresponds to a further reduction in the actual valve opening. The overall characteristics of the compressor at the complete stall point are significantly diminished, and the flow rate is reduced to 2.5 kg/s. The stall groups within the compressor are fully developed at this point, originating primarily from the tip area as depicted in Figure 11 (b). It suggests that the variations in flow structure between the highest efficiency point and stall conditions primarily occur in the tip area, warranting further investigation in this region.

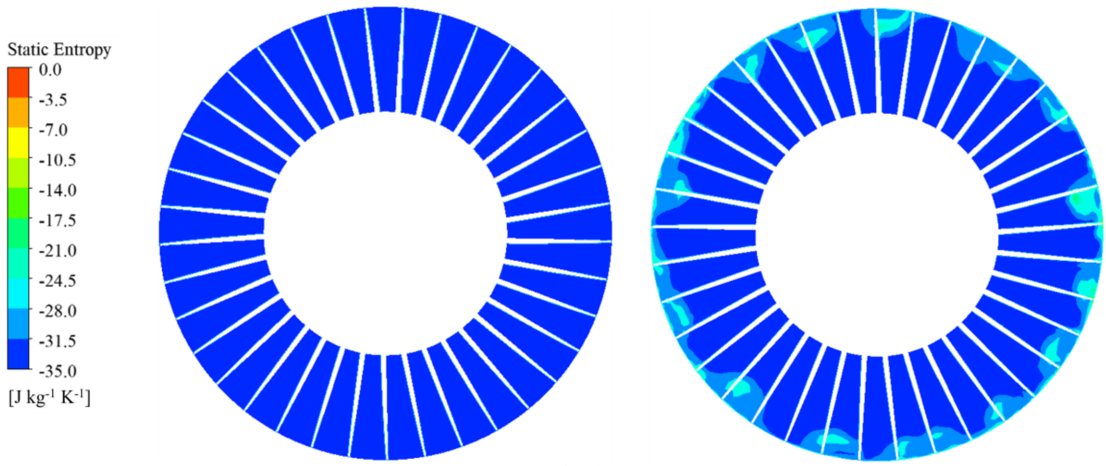

(a) The highest efficiency point. (b) The complete stall point.

Figure 11. Static entropy distributions at rotor inlet.

The static entropy distribution of the rotor in different sections along the flow direction is presented in Figure 12. A tip leakage vortex is formed due to a 0.5 mm gap at the highest efficiency point, indicated by the red line in the figure. The intensity and influence range of the tip leakage vortex is small at the highest efficiency point, but they are significantly amplified at the near-stall point. The time-averaged streamline in the tip area is depicted in Figure 13 to investigate the development of leakage flow in the tip gap further. The blades are labeled as R1 to R3 from left to right for clarity. The tip leakage vortex has a limited range, and only a few streamlines pass through the tip gap of the adjacent blade R2 at the highest efficiency point, as shown by the red solid coil in Figure 13 (a), eventually reaching the gap of R3 (red dotted coil). The leakage flow and tip leakage vortex mix in the channel between R1 and R2 and eventually flow in the main direction. In contrast, the tip leakage vortex is significantly enhanced at the near-stall point, occupying nearly half of the rotor channel. After passing through the tip gap of R1, the leakage flow deviates from the main direction unlike most of the streamlines of the tip leakage vortex, continuing to flow in the circumferential direction. It crosses the tip gap of R2, as illustrated by the red solid coil in Figure 13 (b). A portion of this flow then resumes axial flow in the main direction between R2 and R3, while the remaining portion proceeds through the tip gap of R3 (red dotted coil).

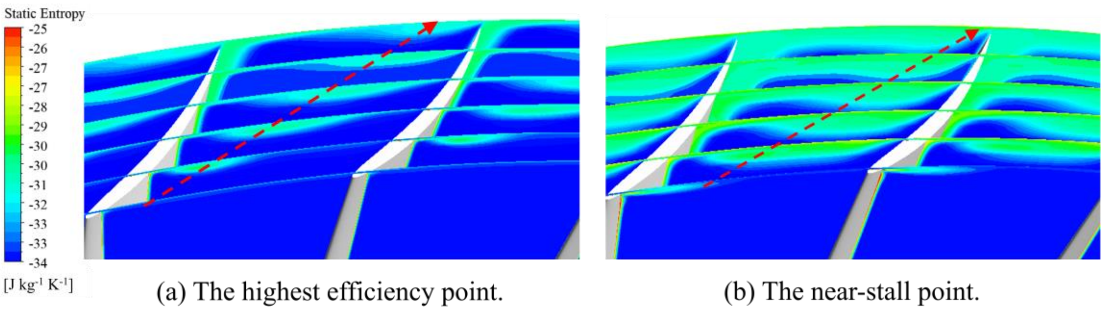

(a) The highest efficiency point. (b) The near-stall point.

Figure 12. Static entropy distributions in the tip area.

The distribution of turbulence kinetic energy at 99.5% span, excluding the guide vane region, illustrates the influence of compressor operation in the near-stall state on the aerodynamic noise source distribution in the tip area, which is a significant parameter for dipole and quadrupole noise sources. The guide vane, having no circumferential bending and span deformation, exhibits low interference intensity with the rotor wake. Therefore, Figure 14 presents the turbulence kinetic energy distributions at the 99.5% span, excluding the guide vane region. The turbulent kinetic energy in the area encompassing approximately 20% to 60% of the chord on the rotor suction surface decreases (within the black circle) as the compressor approaches stall conditions. This reduction implies a potential decrease in the noise source in the rotor tip area at the near-stall point due to variations in the tip area's leakage flow, as indicated in the analysis results of Figure 13. However, this change leads to an increase in the noise source within the stator domain. The enhanced leakage flow in the near-stall point intensifies the interaction between the rotor and stator in the tip region, as observed within the red circle. Consequently, the changes in leakage flow augment the turbulent flow energy in the rotor wake, thereby strengthening the rotor and stator interactions. It ultimately results in a larger noise source on the stator surface.

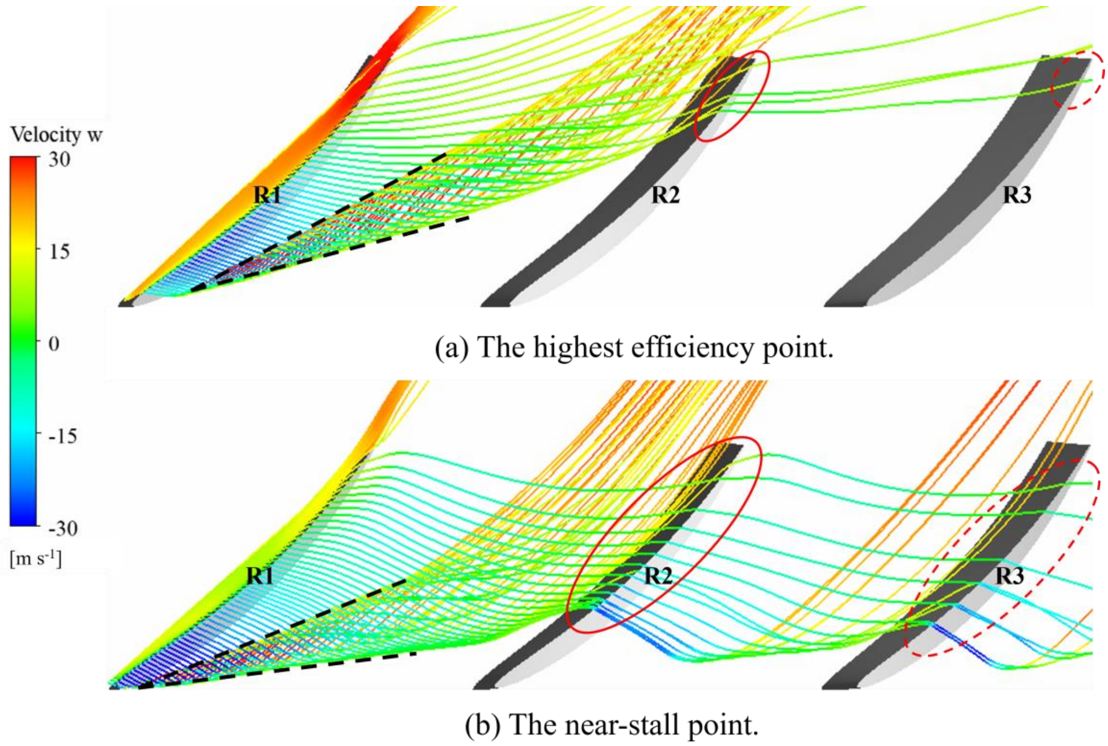

Figure 13. The flow field in tip area.

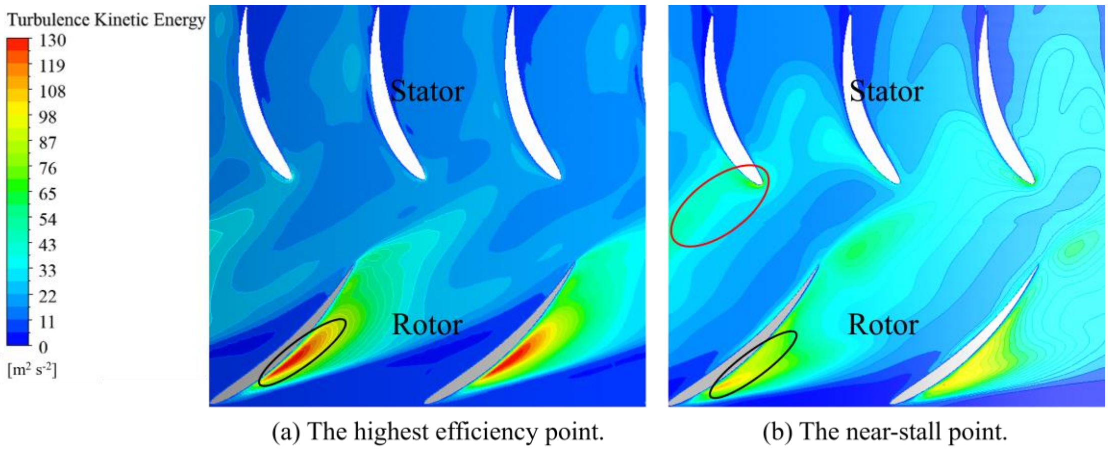

Figure 14. The distributions of turbulence kinetic energy in the tip area.

C. Unsteady flow analysis

The analysis focuses on the unsteady flow characteristics in the tip area of the compressor, considering that noise is a time-varying process, and the variation of static pressure is of utmost interest. Multiple static pressure monitoring points are positioned on the shroud in the unsteady simulation, remaining fixed and not rotating with the mesh in the rotor area, as depicted in Figure 15. These monitoring points, labeled as points 1 to 3, are located at the leading edge, middle of the chord, and trailing edge of the rotor to capture static pressure variations at different positions. The pressure data from the blade rotating two revolutions is collected for analysis once the unsteady simulation reaches convergence. Figure 16 illustrates the temporal evolution of static pressure at these monitoring points. The static pressure at all three measurement points exhibits perfect periodicity at the highest efficiency operating point, with each cycle corresponding to the time taken to complete one rotor revolution. Notably, points 1 and 2 display higher pressure amplitudes compared to point 3, indicating that the flow dynamics influenced by the leakage flow and tip vortex (as shown in Figure 13(a)) primarily impact the front half of the rotor.

However, these characteristics undergo significant changes under the near-stall point. The pressure amplitude at point 3, located at the trailing edge of the rotor, increases, while points 1 and 2 experience a slight decrease. This observation signifies the occurrence of a complex flow phenomenon in the near-stall operating condition. The degree of unsteadiness within the compressor intensifies as the compressor approaches the stall boundary, leading to a deviation from perfect periodicity in the time evolution of static pressure.

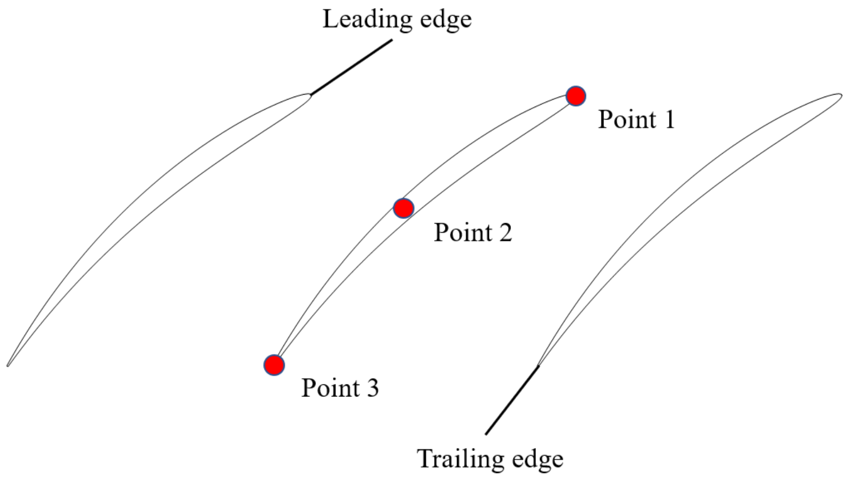

Figure 15. The location of dynamic pressure measurement points.

The frequency characteristics are obtained by applying Fast Fourier Transformation to the static pressures measured at points 1 to 3, as depicted in Figure 17. Distinct peaks appear solely at the BPF and its harmonics, with negligible pressure amplitudes observed at other frequencies at the highest efficiency point, characterized by perfect time periodicity. Points 1 and 2 exhibit significantly higher peaks compared to point 3, consistent with the amplitude in the time domain. The static pressure exhibits prominent peaks not only at the BPF and its harmonics but also at frequencies of 1119 and 2250 Hz at the near-stall point, approximately 0.8 and 1.6 times the BPF, respectively. It indicates that the compressor operating at the near-stall point generates an additional noise source, distinct from the peak frequency associated with the BPF and its harmonics. Similar phenomena have been documented in the research findings of various scholars, with some reporting additional peak frequencies at 0.5 times the BPF (Kameier and Neise, 1997; Galindo *et al.*, 2015), while others at approximately 0.7 times the BPF (Zhu and Carolus, 2018; Zhu *et al.*, 2018). Notably, the amplitude at the trailing edge is significantly greater than at the other two locations for the additional peak frequency. Thus, there is a justifiable reason to infer the presence of a complex flow structure in the tip region of the rotor during near-stall operating conditions.

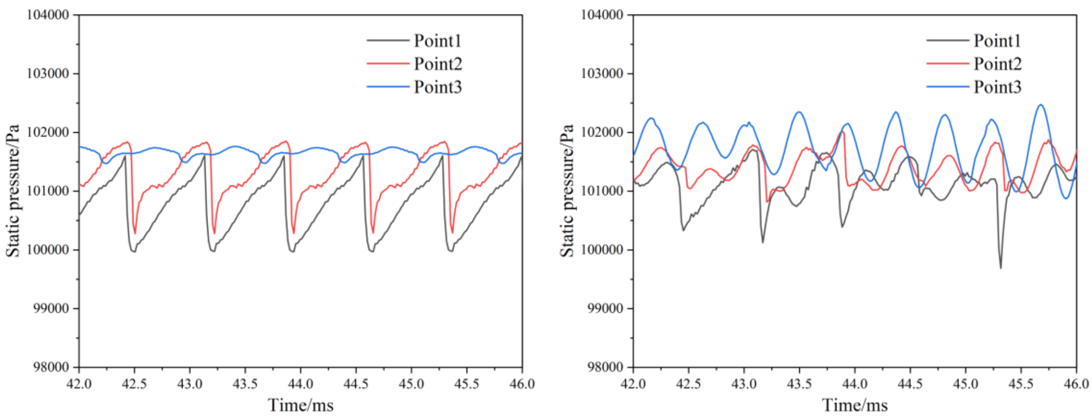

(a) The highest efficiency point. (b) The near-stall point.

Figure 16. The process of static pressure at measurement points.

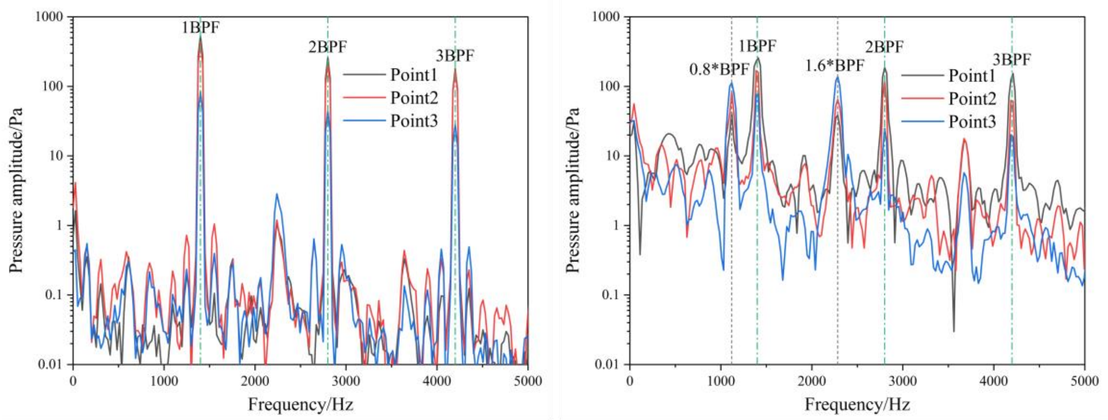

(a) The highest efficiency point. (b) The near-stall point.

Figure 17. Frequency characteristics of static pressure at measurement points.

Figure 18 presents the development of the tip flow field at the near-stall point, illustrated by the negative contour of axial velocity. The time displayed in the figure is scaled by a denominator of 40 times the time step, corresponding to the duration required for one rotor channel rotation. The interval between adjacent contours is set at 20 times the time step, coinciding with half a channel rotation, allowing for the examination of flow structure evolution in the tip region on a larger time scale. Analysis of Figure 18 reveals the presence of four primary regions characterized by backward flow, where the axial velocity is less than 0. These regions include: (i) Region A: Located near the leading edge, generated by the tip clearance vortex. (ii) Region B: Situated near the trailing edge, attributed to radial separation flow causing reverse flow. (iii) Region C: Represents a large low-speed area formed after the merging of regions A and B. (iv) Region D: Originates from the development of region C and is subsequently severed by the leading edge of the adjacent blade. Region D progresses downstream within the blade passage and eventually dissipates. The identified regions contribute to the overall understanding of the flow behavior within the tip region, providing valuable insights into the complex flow dynamics occurring at the near-stall operating point.

At the time corresponding to 0/40 T, the generation of backflow regions A and B by the tip leakage vortex and radial separation flow occurs at the leading and trailing edge of the rotor, respectively. Confirmation of region B's origin from the radial separation flow is depicted by the streamlines shown in Figure 19, which are associated with region B and emanate from the vicinity of the hub near the rotor suction surface. By 20/40 T, a tendency of mixture arises as region A propagates towards the trailing edge, leading to the blending of regions A and B. Subsequently, the combination of regions A and B gives rise to the formation of a large low-speed region C within the rotor channel at 40/40 T. Region C progresses towards the leading edge of the adjacent blade at 60/40 T, eventually engaging in interaction with the adjacent blade. Region C divides into two reverse flow regions at 80/40 T, namely A and a merged region D (region D and region B are mixed and difficult to distinguish at this moment). Additionally, region A manifests near the leading edge of the adjacent blade. Regions B and D inevitably split into two distinct parts at 100/40 T, as the location of radial separation flow generation remains unchanged, and region D continues to develop downstream. Concurrently, the severed region A develops backward at the leading edge of the adjacent blade, anticipated to merge with the adjacent blade's region B. The backflow velocity within region D gradually diminishes during the subsequent intervals of 120/40 T and 140/40 T, dissipating continuously as the channel evolves. Simultaneously, region A persists in backward development until eventually merging with region B, generating a large low-speed region C within the adjacent rotor.

The multitude of reverse flow regions of varying sizes is formed in the rotor channel as the outlet pressure of the compressor is increased, resulting in the development of a complex flow in the rotor's tip area. These reverse flow regions ultimately contribute to the occurrence of compressor stall. The presence of these regions not only significantly impacts the aerodynamic performance of the compressor but also leads to the emergence of numerous low-speed clusters that interact with the rotor blades. The existence of these low-speed clusters has dual consequences. Firstly, it imposes an augmented load on the blade surface, intensifying the aerodynamic noise sources of the compressor, particularly the dipole sources. Secondly, the interaction between the low-speed clusters and the rotor blades gives rise to new interference frequencies in the spectrum, causing changes in the noise frequency characteristics of the compressor and introducing additional noise sources (as evidenced by the peaks at 0.8 times and 1.6 times the BPF in Figure 17).

Figure 20 illustrates the tip flow field at the highest efficiency point, revealing the absence of any discernible recirculation structure in the rotor tip area. The figure specifically displays the speed distribution of the rotor at 0/40 T and 140/40 T, as the contours at different time instances exhibit a high degree of similarity. The flow within the channel appears remarkably smooth and unobstructed, in stark contrast to the velocity distribution observed at the near-stall point.

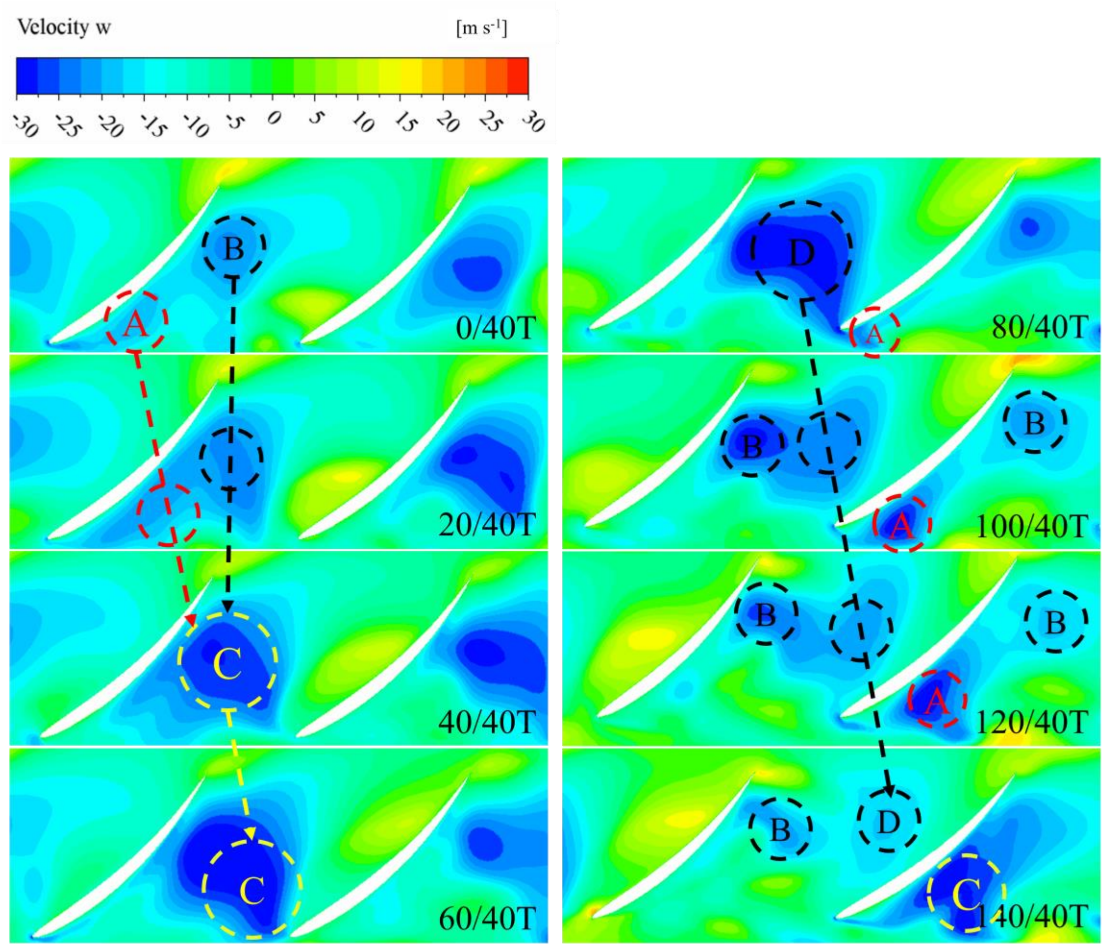

Figure 18. The development process of the flow structure in the tip area in near-stall point.

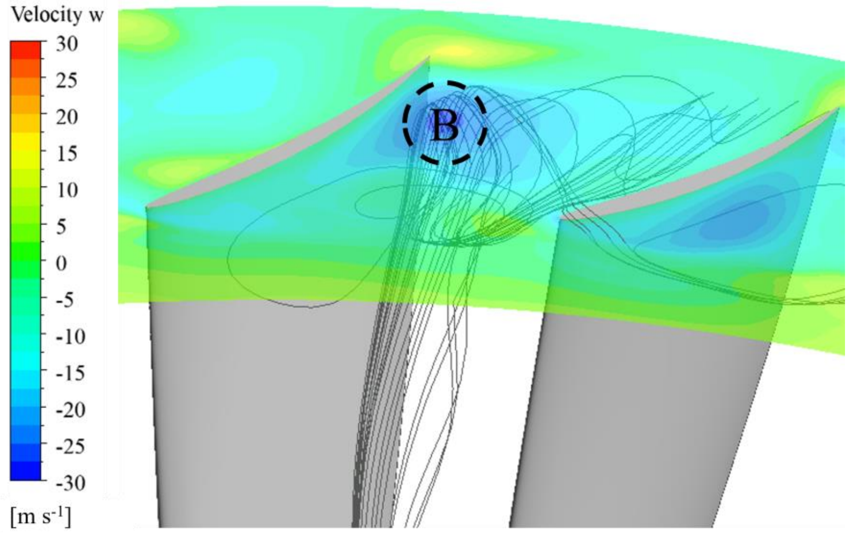

Figure 19. The structure of radial separation flow at near-stall point.

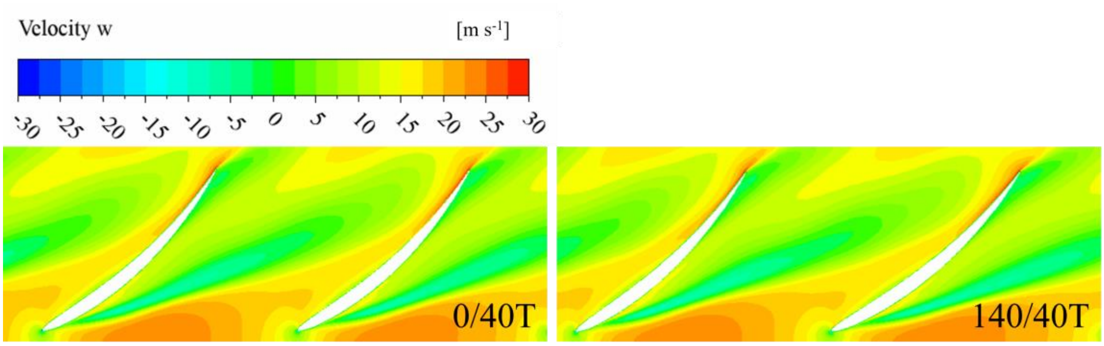

Figure 20. The process of flow structure in the tip area at highest efficiency point.

D. Aerodynamic noise sources and free-field acoustic responses

The direct indicators of machine noise intensity are undoubtedly the intensity of the noise source and the radiated sound power in free-field in noise analysis. The distribution of the noise source in the impeller area is calculated using aerodynamic noise theory in this study, while the noise propagation in free-field is simulated using the obtained noise source. Both calculations do not involve complex structures that can reflect or diffract noise, thereby providing a direct representation of the noise generated under different working conditions. The rotor-stator interaction, acknowledged as the principal mechanism of aerodynamic noise (Lewis *et al.*, 2022), contributes as a surface noise source based on the weak variational form of Lighthill's theory in Section 2.3 and the surface source schematic diagram presented in Figure 6. Consequently, the distribution of surface noise sources at the rotor-stator interface serves as a reflection of both the strength of the rotor-stator interaction and a crucial basis for assessing the intensity of the aerodynamic noise source.

The primary focus lies on the source of typical single-tone noise. The intensity distribution of the noise source for the first two orders of BPF in the rotor-stator interface is depicted in Figure 21, with a display range spanning from 80 to 105 dB. The most significant variation is observed in the outer circle beyond 30% of the radius, exhibiting an approximately 6 dB difference comparing the surface noise source distribution under the highest efficiency and near-stall working conditions. The disparity in the intensity of the noise source is minimal in the inner ring below 30% of the radius, with an approximate value of 2 dB. It indicates that the effect of rotor-stator interaction in the compressor is indeed intensified at the near-stall point, resulting in an increased aerodynamic noise source associated with typical single-tone noise. Furthermore, the impact on the noise source distribution at the near-stall point predominantly concentrates in the outer ring at the higher radius, aligning with the preceding analysis of flow structures, as the complex flow at the near-stall point originates from the rotor's tip area.

Subsequently, the analysis focuses on the distribution and disparity of aerodynamic noise sources corresponding to the additional peak frequencies obtained in Figure 17. Figure 22 presents the findings. A substantial discrepancy is observed in the intensity of the noise source at the rotor-stator interface, surpassing that at the BPF and its harmonics since the normally operating compressor where no additional peak frequencies are generated (as depicted in Figure 17(a)). The noise source under the near-stall condition is approximately 20 dB greater than that under the highest efficiency point at 0.8 times BPF, while the disparity at 1.6 times BPF exceeds 10 dB as well. Undoubtedly, these two additional frequencies will manifest as new noise sources for the compressor during operation at the near-stall point.

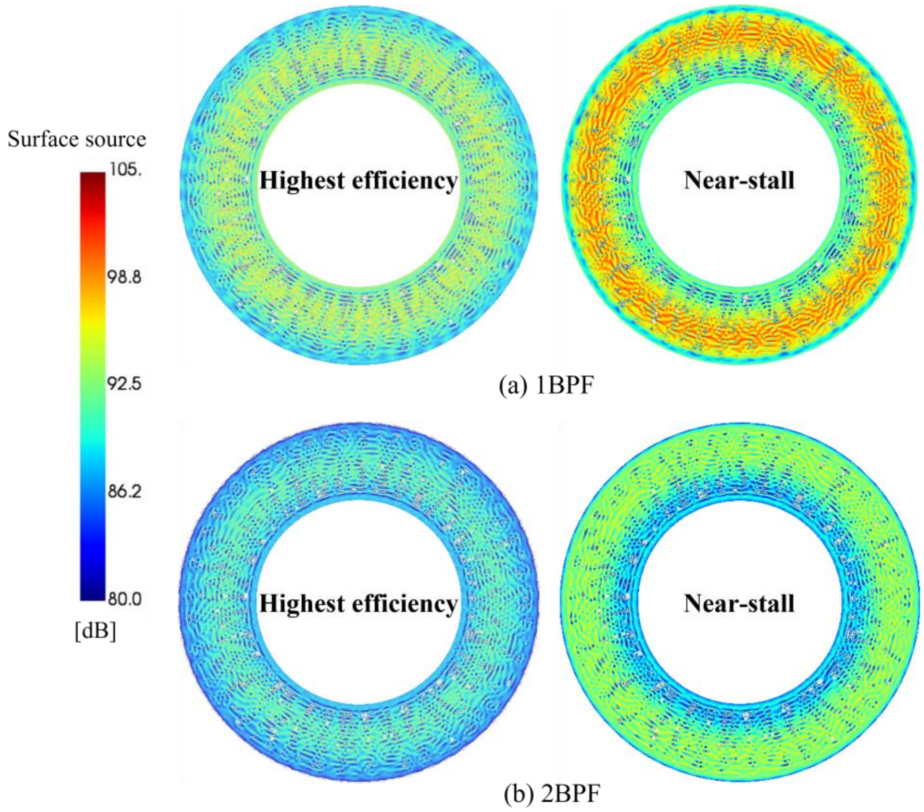

Figure 21. The intensity of surface noise source at 1BPF and 2BPF in rotor-stator interface.

The discrepancy in volume sources of the stator under the two operational conditions is depicted in Figure 23. Variances between the highest efficiency point and the near-stall point are similarly identified. Under 0.8 times BPF, heightened noise source intensity at the highest efficiency point is exclusively distributed within the region encompassing the stator, while near the stall point, elevated noise source intensity permeates the entire stator calculation domain, encompassing the stator wake area. This variability undergoes a substantial reduction at 1.6 times BPF. In general, the noise source intensity at the highest efficiency point remains inferior to that near the stall point, with the most pronounced noise source situated on the stator surface. The observation suggests that the dipole noise source, resulting from rotor-stator interaction, prominently manifests as the primary compressor noise source, specifically distributed on the stator surface.

Finally, Figure 24 presents the sound power responses in free-field for the highest efficiency and near-stall conditions. The radiated sound power in free-field is computed using the FW-H equation (Williams and Hawkings, 1969), while the evaluation of the compressor's total noise intensity relies on the radiated sound power on a spherical surface encompassing the compressor impeller. The typical single-tone noise at the near-stall point surpasses that at the highest efficiency point. Specifically, the discrepancy is 3.2 dB at 1BPF, and 2.1 dB and 0.5 dB at 2BPF and 3BPF, respectively. However, the difference in radiated sound power level is comparatively significant at the two additional frequencies (0.8 and 1.6 times BPF), particularly at 0.8 BPF, reaching as high as 33.3 dB. The peak value of 0.8 and 1.6 times BPF is as high as 80 dB, second only to that of 1BPF, equivalent to the peak values of 2BPF and 3BPF, thereby constituting an important noise source for the compressor at the near-stall point. Furthermore, the broadband noise emitted by the compressor at the near-stall point is significantly greater than that at the highest efficiency point. The total sound power levels in free-field for the compressor at the highest efficiency and near-stall points are 110.5 dB and 119.3 dB, respectively. The single-tone noise and broadband noise originating from the near-stall point exceed those at the highest efficiency point, with the single-tone noise corresponding to 0.8 times BPF exhibiting a substantial increase. These findings are consistent with the conclusions drawn from the flow field analysis. The two additional peak frequencies resulting from the complex flow indeed serve as new noise sources for the compressor at the near-stall point, and their impact cannot be overlooked, as they make a crucial contribution to the overall noise level.

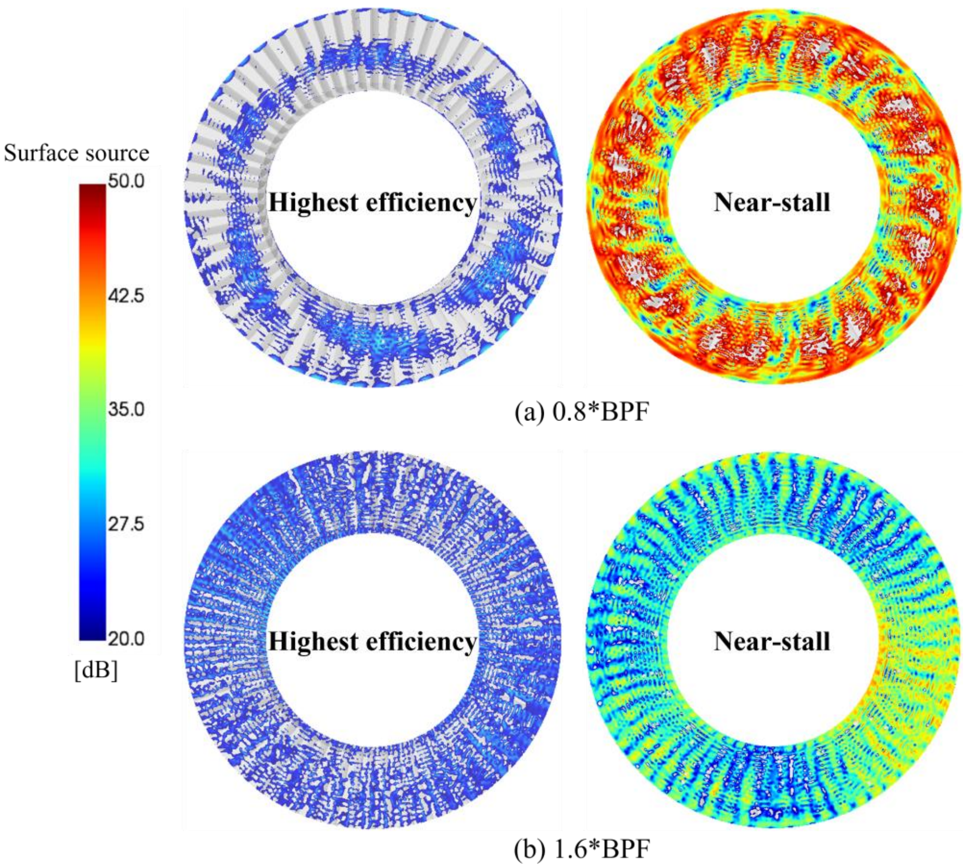

Figure 22. The intensity of surface noise source at 0.8*BPF and 1.6*BPF in the rotor-stator interface.

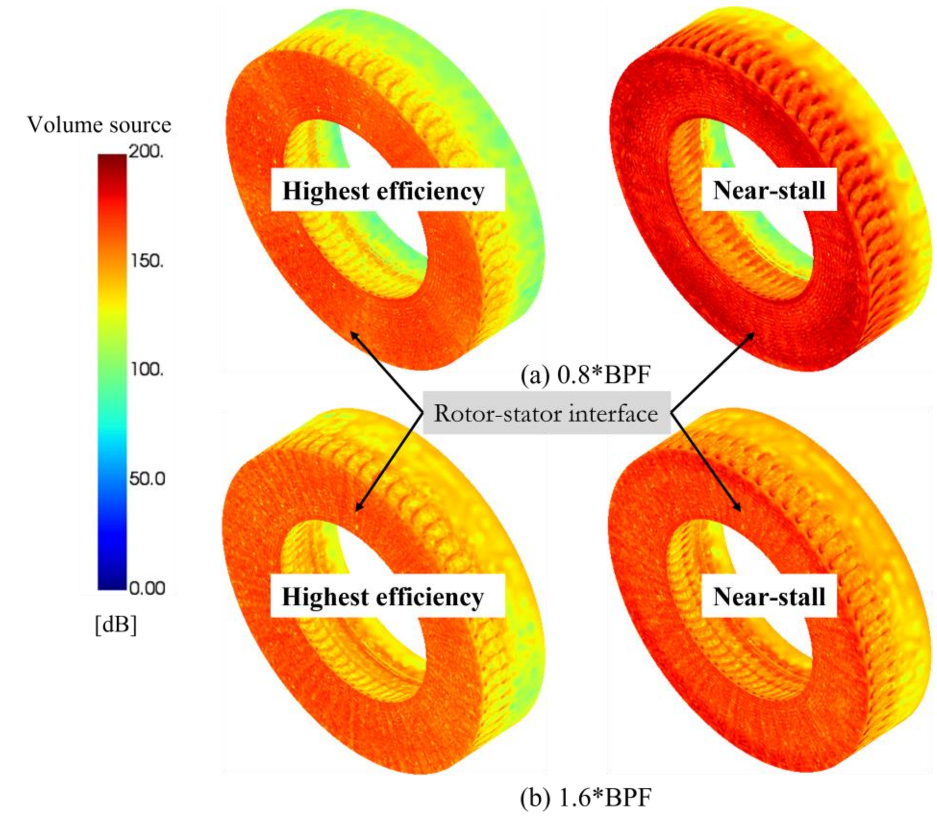

Figure 23. The intensity of volume noise source at 0.8*BPF and 1.6*BPF in the stator.

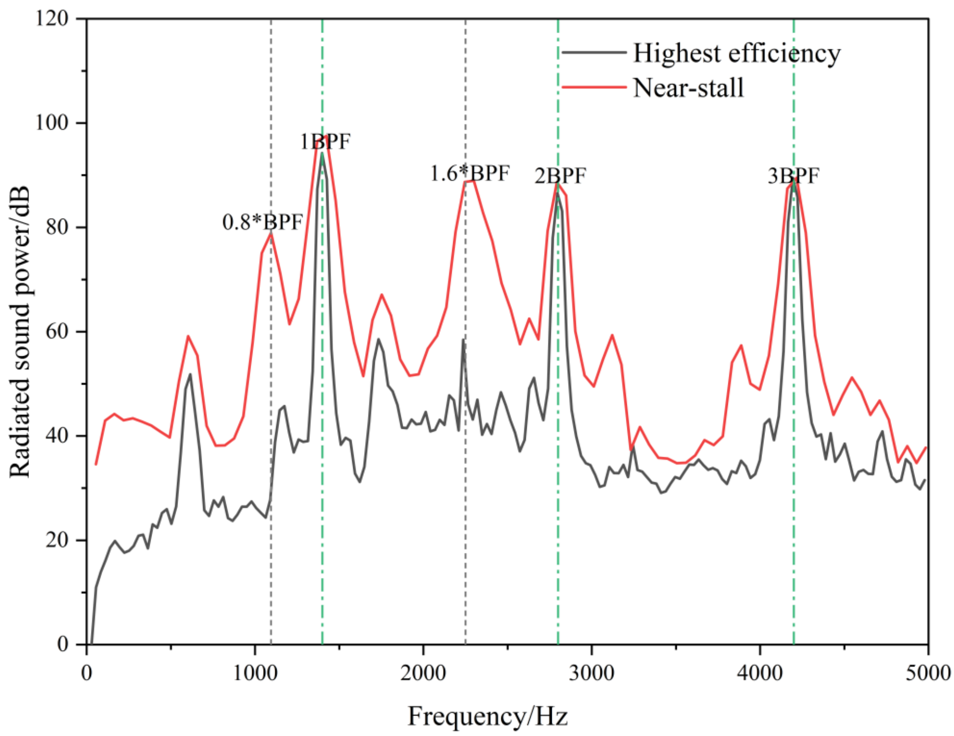

Figure 24. The radiated sound power in free-field.

E. Actual duct acoustic response

The noise analysis in the actual duct utilizes the mesh depicted in Figure 6, and Figure 25 illustrates the noise spectrum obtained from numerical simulations of the five measurement points situated in the inlet plane shown in Figure 8. The Distribution at the inlet plane is approximate axisymmetric regarding the BPF and its harmonics. Notably, Point 3, which faces the center of the inlet, registers the highest SPL at the BPF and its harmonics, while Points 1 and 5, located farthest from the axis (with a 90-degree angle between the line connecting the monitoring point and the center of the inlet plane and the compressor axis), exhibit the lowest SPL. Concerning 0.8 and 1.6 times BPF, the radiation lobe of noise at the inlet is biased towards the side encompassing Points 4 and 5. Points 3, 4, and 5 showcase the highest peaks at these two frequencies, whereas Points 1 and 2 display the smallest peaks. Figure 26 presents a comparison of the total SPL of the compressor under the highest efficiency and near-stall conditions. Irrespective of the working condition, the total SPL at the compressor's inlet plane also demonstrates an approximate axisymmetric distribution, with the noise level at the near-stall operating point averaging around 6 dB higher than that at the highest efficiency point. This observation underscores that the noise experiences a relatively substantial increase under extreme conditions even within the actual duct.

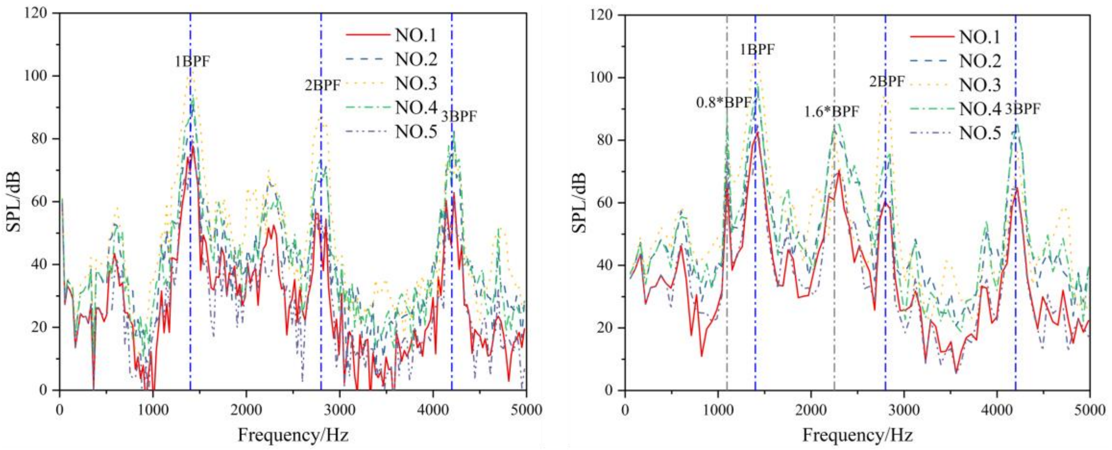

(a) The highest efficiency point. (b) The near-stall point.

Figure 25. Noise spectrum of measurement points of the inlet plane.

A detailed comparison of the noise spectrum predicted at point 3 under different operating conditions is depicted in Figure 27. It becomes evident that the acoustic response of the compressor noise, after propagating through the actual duct, closely resembles that of the free-field when considering the spectrum of free-field radiated sound power in Figure 24. However, at 0.8 and 1.6 times BPF, the noise propagation at the near-stall point experiences suppression due to a significant reduction in the disparity between the near-stall point and the highest efficiency point at these frequencies. More specifically, the difference at 0.8 times BPF amounts to approximately 10 dB, while the disparity decreases to 7 dB at 1.6 times BPF. A preliminary evaluation of the sound propagation in the actual duct is obtained using

$$f_{mn} = \sqrt{1 - M^2} \frac{\alpha_{mn} c}{2\pi a} \tag{22}$$

to calculate the cut-off frequencies of the higher-order modes. In Equation (22), f_{mn} is the cut-off frequency of the m-th order circumferential and n-th order radial modes, M is the Mach number corresponding to the axial velocity, α_{mn} is the nth zero point of the derivative of the m-th order Bessel function of the annular duct, c is the speed of sound, and a is the outer radius.

A mode can propagate in the duct when the frequency of interest exceeds the duct's cut-off frequency according to the duct acoustics theory (Jacobsen and Juhl, 2013). The focal point of this study revolves around the additional peak frequencies, specifically the frequencies of 0.8 and 1.6 times BPF. The velocity is approximately 22.1 m/s at the near-stall point. An analysis is conducted to determine the cut-off frequencies for various modes at the near-stall point by employing the parameters presented in Table I, and the results are outlined in Table IV. Regarding the frequency of 0.8 times BPF, the highest circumferential mode order capable of propagation is 3, while no higher-order modes in the radial direction are excited, as demonstrated in the shaded region in Table IV. On the other hand, the maximum circumferential mode order that can propagate in a practical annular duct reaches 7 for the frequency of 1.6 times BPF. Only a mode order of 1 can propagate in terms of the radial direction. Consequently, a majority of the higher-order modes are attenuated, providing a partial explanation for the distinctions observed between the free-field response and the practical duct acoustic response at 0.8 and 1.6 times BPF in a real duct configuration.

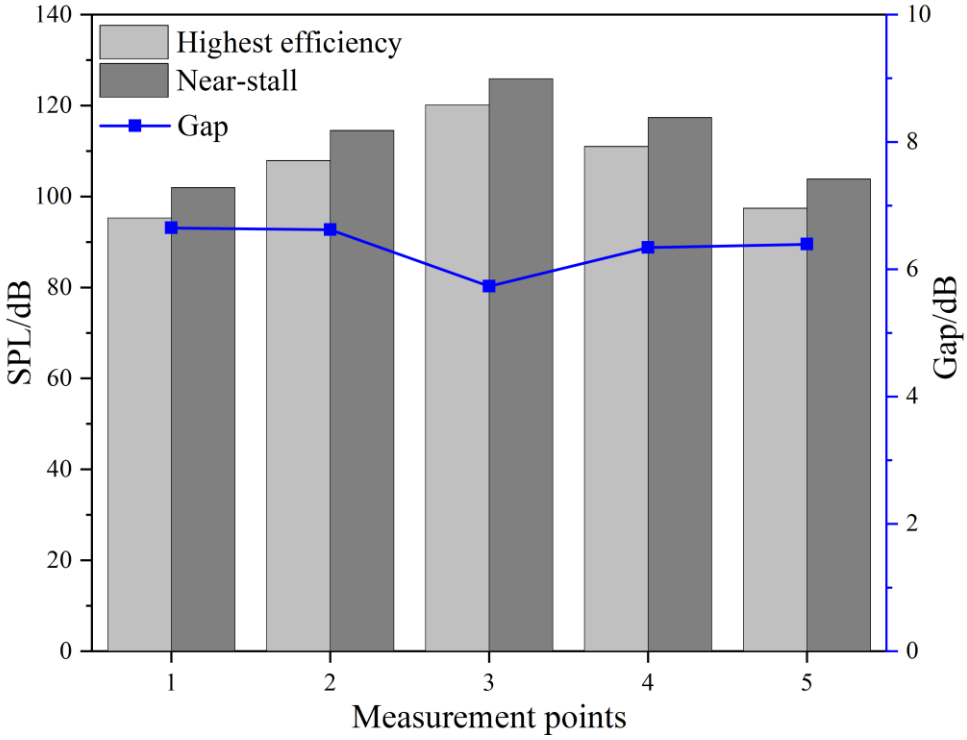

Figure 26. The SPL comparison of the measuring points.

To conduct a comparative analysis of the noise distribution at the entrance of the compressor, the SPL distribution of the typical 0.8 times BPF and the BPF is selected for examination, as depicted in Figure 28. The SPL distribution exhibits striking similarity under different working conditions in the case of the BPF, with only slight variations observed in the magnitude of the radiated sound lobe. Conversely, the radiation lobes of the near-stall point differ entirely from those of the highest efficiency point (both in terms of the number of lobes and the orientation of the main lobe) at 0.8 times BPF, signifying a substantial alteration in the radiation characteristics of the entrance.

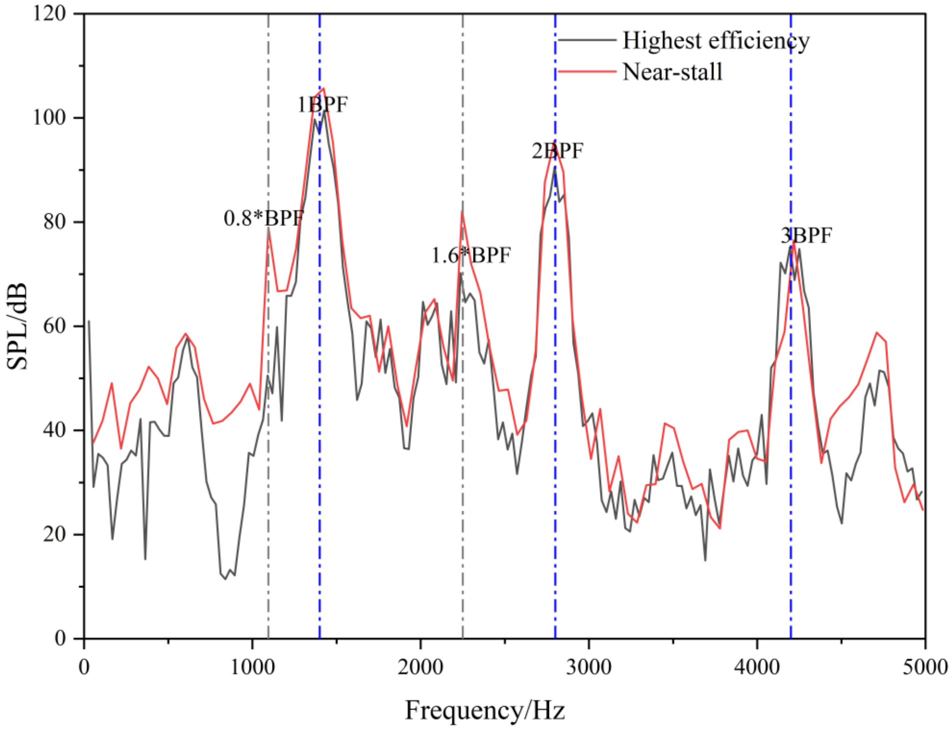

Figure 27. Noise spectrum comparison of measuring point 3.

Table IV. The cut-off frequency at the near-stall point.

Mode (m, n)	Cut-off frequency/Hz	Mode (m, n)	Cut-off frequency/Hz
(1,0)	311.9	(5,0)	1483.4
(2,0)	619.3	(0,1)	1602.7
(3,0)	918.2	(6,0)	1751.3
(4,0)	1206.3	(7,0)	2012.1

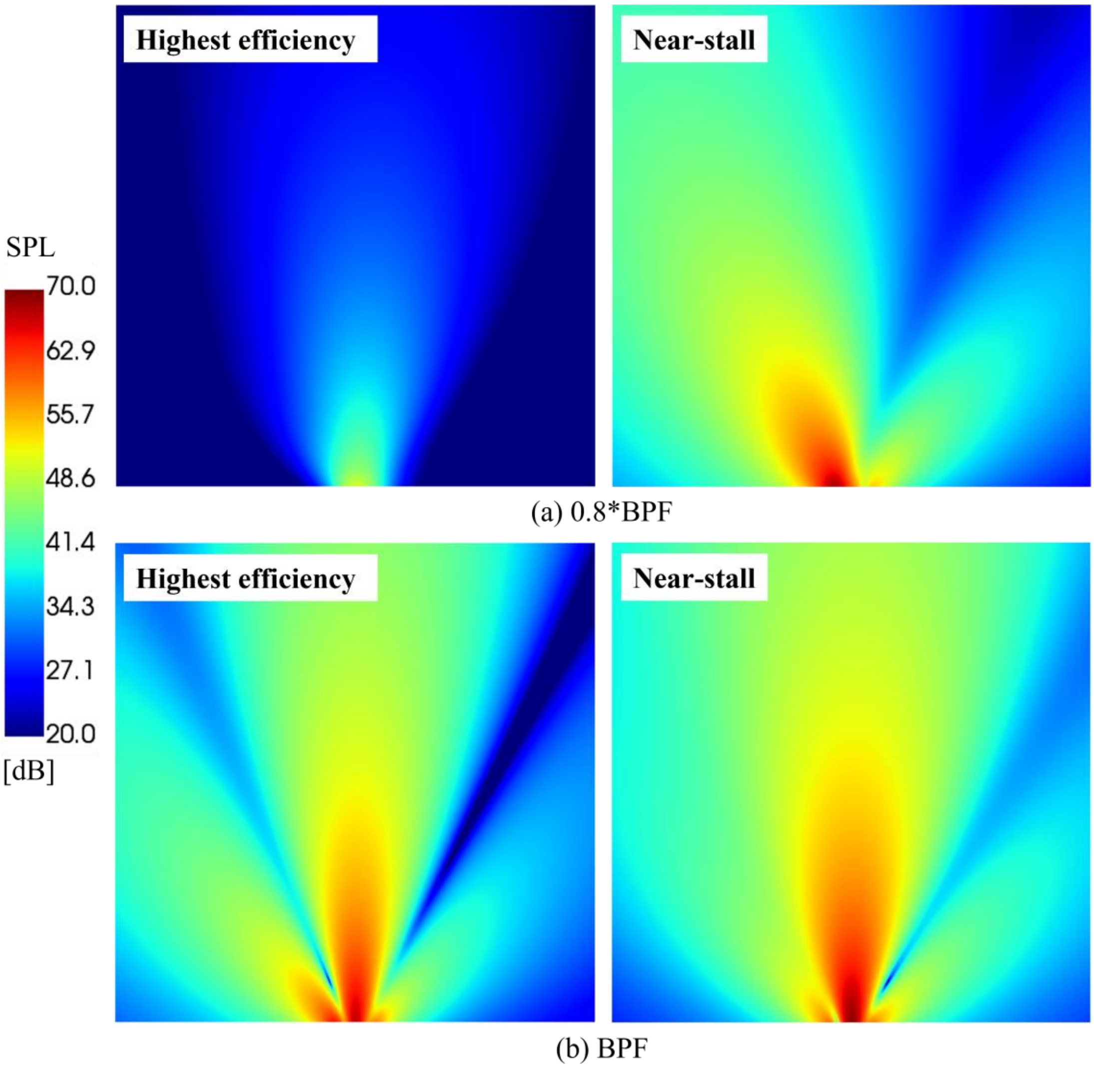

Figure 28. SPL distribution at the entrance.

IV. CONCLUSIONS

In this paper, a hybrid method combining Computational Fluid Dynamics and Finite Element Method was employed to investigate the flow field and aerodynamic noise of a maritime 1.5-stage axial compressor operating at both highest efficiency and near-stall points. The focus was on discussing the differences in flow characteristics and noise response between these two operating conditions. Our research significantly expands the understanding of aerodynamic noise in 1.5-stage compressors under near-stall conditions, an area that has previously received limited numerical investigation. The numerical approach used in this study has been previously validated through experimental analysis.

The key findings of this investigation can be summarized as follows:

A comparison of steady flow parameters at the highest efficiency and near-stall points revealed that the primary change in flow structure occurs in the rotor's tip region. The extent and magnitude of leakage flow and tip leakage vortex are greater at the near-stall point, altering the distribution of turbulent kinetic energy associated with noise within the tip area.

A significant difference was observed at the near-stall point, where two extra peak frequencies emerged, specifically 0.8 and 1.6 times the Blade Passage Frequency. In addition to peaks corresponding to the Blade Passage Frequency and its harmonics within the frequency spectrum of pressure fluctuations in the tip region, a detailed examination of flow phenomena within the tip area at the near-stall point was conducted to comprehensively describe the flow structure associated with these additional peak frequencies.

The analysis of the surface source presentation reveals an observed elevation in the intensity of the noise source at the near-stall point during the Blade Passage Frequency and its harmonics, with the most prominent amplification of the noise source evident at the two supplementary peak frequencies. This finding is further corroborated by the examination of the radiated sound power spectrum in the free-field, unequivocally demonstrating that the additional peaks have assumed a crucial role as noise sources for the compressor at the near-stall operating point.

Finally, a comprehensive investigation was conducted to examine the acoustic response of the compressor in the actual duct, which revealed an average increase of 6 dB in noise levels at the near-stall point. Notably, the distribution of noise at the compressor inlet during the Blade Passage Frequency and its harmonics exhibited an approximate axisymmetric pattern. However, a distinct disparity was observed in the noise distribution between the highest efficiency and near-stall points at the additional peak frequencies. Specifically, the presence of single-tone noise with extra peak frequencies appeared to be attenuated within the duct, possibly due to the limited number of propagable acoustic modes in the annular duct.

ACKNOWLEDGMENT

This work was supported by Fundamental Research Funds for the Central

Universities (3072022TS0307) and the National Science and Technology Major Project (HT-J2019-Ⅱ-0013-0034).

AUTHOR DECLARATIONS

The authors declare no conflict of interest in preparing this article.

DATA AVAILABILITY

The data that support the findings of this study are available from the corresponding author upon reasonable request.

REFERENCES

Anand, Y., Verma, S. K., Anand, S., and Ashrae (**2018**). "Transient 3-D modelling of ceiling fan for achieving thermal comfort," in *Building Performance Analysis Conference and SimBuild* (Chicago, LA), pp. 197-204.

Avallone, F., Ragni, D., and Casalino, D. (**2020**). "On the effect of the tip-clearance ratio on the aeroacoustics of a diffuser-augmented wind turbine," Renewable Energy **152**, 1317-1327.

Baumgartner, M., Kameier, F., and Hourmouziadis, J. (**1995**). "Non-engine order blade vibration in a high pressure compressor," in *Proceedings of the 12th International Symposium on Air Breathing Engines. Part 2 (of 2), Sep 10 - 15 1995* (AIAA, Melbourne, Aust), pp. 1019-1019.

Boulamatsis, A. M., Barlas, T. K., and Stapountzis, H. (**2019**). "Active control of wind turbines through varying blade tip sweep," Renewable Energy **131**, 25-36.

Brandstetter, C., Paoletti, B., and Ottavy, X. (**2019**). "Compressible modal instability onset in an aerodynamically mistuned transonic fan," Journal of Turbomachinery-Transactions of the Asme **141**.

Broatch, A., Galindo, J., Navarro, R., Garcia-Tiscar, J., Daglish, A., and Sharma, R. K. (**2015**). "Simulations and measurements of automotive turbocharger compressor whoosh noise," Engineering Applications of Computational Fluid Mechanics **9**, 12-20.

Casalino, D., Grande, E., Romani, G., Ragni, D., and Avallone, F. (**2021**). "Towards the definition of a benchmark for low Reynolds number propeller aeroacoustics," in *18th International Symposium on Transport Phenomena and Dynamics of Rotating Machinery, ISROMAC 2020* (Institute of Physics).

Casalino, D., van der Velden, W. C. P., Romani, G., and Gonzalez-Martino, I. (**2019**). "Aeroacoustic analysis of urban air operations using the lb/vles method," in *25th AIAA/CEAS Aeroacoustics Conference, 2019, May 20, 2019 - May 23, 2019* (American Institute of Aeronautics and Astronautics Inc, AIAA, Delft, Netherlands).

Celik, I. B., Ghia, U., Roache, P. J., Freitas, C. J., Coleman, H., and Raad, P. E. (**2008**). "Procedure for estimation and reporting of uncertainty due to discretization in CFD applications," Journal of Fluids Engineering, Transactions of the ASME **130**, 0780011-0780014.

Cudina, M. (**2001**). "Noise generation in vane axial fans due to rotating stall and surge," Proceedings of the Institution of Mechanical Engineers, Part C: Journal of Mechanical Engineering Science **215**, 57-64.

Day, I. J., and Asme (**2015**). "Stall, surge and 75 years of research," in *ASME Turbo Expo: Turbine Technical Conference and Exposition* (Montreal, CANADA).

Dehner, R., Selamet, A., Sriganesh, P., Banerjee, D., Selamet, E., Karim, A., Brewer, T., and Morelli, A. (**2022**). "Physical insight into whoosh noise in turbocharger compressors using computational fluid dynamics," in *ASME Turbo Expo 2022: Turbomachinery Technical Conference and Exposition, GT 2022, June 13, 2022 - June 17, 2022* (American Society of Mechanical Engineers (ASME), Rotterdam, Netherlands), p. International Gas Turbine Institute.

Du, J., Lin, F., Zhang, H., and Chen, J. (**2008**). "Numerical simulation on the effect of tip clearance size on unsteadiness in tip clearance flow," Journal of Thermal Science **17**, 337-342.

Fukano, T., and Jang, C. M. (**2004**). "Tip clearance noise of axial flow fans operating at design and off-design condition," Journal of Sound and Vibration **275**, 1027-1050.

Galindo, J., Tiseira, A., Navarro, R., and Lopez, M. A. (**2015**). "Influence of tip clearance on flow behavior and noise generation of centrifugal compressors in near-surge conditions," International Journal of Heat and Fluid Flow **52**, 129-139.

Hu, B.-B., Ouyang, H., Wu, Y.-D., Jin, G.-Y., Qiang, X.-Q., and Du, Z.-H. (**2013**). "Numerical prediction of the interaction noise radiated from an axial fan," Applied Acoustics **74**, 544-552.

Ianniello, S. (**2020**). "The K-Algorithm and the modeling of the emission surface from supersonically rotating bodies," Journal of Computational Physics **408**.

Jacobsen, F., and Juhl, P. M. (**2013**). *Fundamentals of general linear acoustics* (John Wiley & Sons).

Kameier, F., and Neise, W. (**1997**). "Rotating blade flow instability as a source of noise in axial turbomachines," Journal of Sound and Vibration **203**, 833-853.

Karstadt, S., Hess, M., Matyschok, B., Pelz, P. F., and Asme (**2010**). "The influence of tip clearance on the acoustic and aerodynamic characteristics of fans," in *ASME Turbo Expo 2010* (Glasgow, SCOTLAND), pp. 39-47.

Kholodov, P., and Moreau, S. (**2021**). "Identification of Noise Sources in a Realistic Turbofan Rotor Using Large Eddy Simulation," in *18th International Symposium on Transport Phenomena and Dynamics of Rotating Machinery, ISROMAC 2020* (Institute of Physics).

Kierkegaard, A., West, A., and Caro, S. (**2016**). "HVAC noise simulations using direct and hybrid methods," in *22nd AIAA/CEAS Aeroacoustics Conference, 2016, May 30, 2016 - June 1, 2016* (American Institute of Aeronautics and Astronautics Inc, AIAA, Lyon, France).

Kraxberger, F., Kurz, E., Weselak, W., Kubin, G., Kaltenbacher, M., and Schoder, S. (**2023**). "A validated finite element model for room acoustic treatments with edge absorbers," Acta Acustica **7**.

Lasota, M., idlof, P., Maurerlehner, P., Kaltenbacher, M., and Schoder, S. (**2023**). "Anisotropic minimum dissipation subgrid-scale model in hybrid aeroacoustic simulations of human phonation," Journal of the Acoustical Society of America **153**, 1052-1063.

Lewis, D., Moreau, S., Jacob, M. C., and Sanjose, M. (**2022**). "ACAT1 Fan Stage Broadband Noise Prediction Using Large-Eddy Simulation and Analytical Models," Aiaa Journal **60**, 360-380.

Li, H., Zheng, Q., Chen, Z., Duan, Y., Jiang, B., and Benini, E. (**2021**). "The role of radial secondary flow in the process of rotating stall for a 1.5-stage axial compressor," Aerospace Science and Technology **115**.

Lighthill, M. J. (**1952**). "On sound generated aerodynamically I. General theory," Proceedings of the Royal Society of London. Series A. Mathematical Physical Sciences **211**, 564-587.

Lu, H., Xiao, Y., Liu, Z., and Yuan, Y. (**2022**). "Simulation and experimental research on aerodynamic noise of gas turbine 1.5-stage axial compressor," Applied Acoustics **192**, 108722.

Lu, H., Xiao, Y., Liu, Z., Yuan, Y., and Zhou, P. (**2023**). "The effect of tip clearance on the rotor-stator interaction and noise of marine 1.5-stage compressor," Journal of Marine Engineering & Technology **23**, 33-46.

Maaloum, A., Kouidri, S., and Rey, R. (**2004**). "Aeroacoustic performance evaluation of axial flow fans based on the unsteady pressure field on the blade surface," Applied Acoustics **65**, 367-384.

Mailach, R., Lehmann, I., and Vogeler, K. (**2001**). "Rotating instabilities in an axial compressor originating from the fluctuating blade tip vortex," Journal of Turbomachinery **123**, 453-463.

Marz, J., Hah, C., and Neise, W. (**2002**). "An experimental and numerical investigation into the mechanisms of rotating instability," Journal of Turbomachinery-Transactions of the Asme **124**, 367-374.

Menter, F. R. (**1994**). "Two-equation eddy-viscosity turbulence models for engineering applications," AIAA journal **32**, 1598-1605.

Moghadam, S. M. A., Meinke, M., and Schroeder, W. (**2019**). "Numerical analysis of the acoustic field of a ducted axial fan at varying tip clearances," Acta Acustica United with Acustica **105**, 43-55.

Oberai, A. A., Roknaldin, F., and Hughes, T. J. R. (**2000**). "Computational procedures for determining structural-acoustic response due to hydrodynamic sources," Computer Methods in Applied Mechanics and Engineering **190**, 345-361.

Oberai, A. A., Roknaldin, F., and Hughes, T. J. R. (**2002**). "Computation of trailing-edge noise due to turbulent flow over an airfoil," AIAA Journal **40**, 2206-2216.

Pardowitz, B., Tapken, U., Neuhaus, L., and Enghardt, L. (**2015**). "Experiments on an axial fan stage: Time-resolved analysis of rotating instability modes," Journal of Engineering for Gas Turbines and Power **137**.

Pardowitz, B., Tapken, U., Sorge, R., Thamsen, P. U., and Enghardt, L. (**2014**). "Rotating instability in an annular cascade: Detailed analysis of the instationary flow phenomena," Journal of Turbomachinery **136**.

Polacsek, C., Burguburu, S., Redonnet, S., and Terracol, M. (**2006**). "Numerical simulations of fan interaction noise using a hybrid approach," AIAA Journal **44**, 1188-1196.

Pullan, G., Young, A. M., Day, I. J., Greitzer, E. M., and Spakovszky, Z. S. (**2015**). "Origins and structure of spike-type rotating stall," Journal of Turbomachinery **137**.

Ren, K.-X., Shuai, Z.-J., Wang, X., Jian, J., Yu, T., Dong, L.-Y., Li, W.-Y., and Jiang, C.-X. (**2022**). "Aerodynamic noise prediction of a high-speed centrifugal fan considering impeller-eccentric effect," Engineering Applications of Computational Fluid Mechanics **16**, 780-803.

Sajadmanesh, S. M., Mojaddam, M., Mohseni, A., and Nikparto, A. (**2019**). "Numerical identificaticin of separation bubble in.an ultra-high-lift turbine cascade using URANS simulation and proper orthogonal decomposition," Aerospace Science and Technology **93**.

Sanjose, M., Hub, S., Lorcher, F., and Moreau, S. (**2021**). "Noise mechanisms in a radial fan without volute," in *18th International Symposium on Transport Phenomena and Dynamics of Rotating Machinery, ISROMAC 2020* (Institute of Physics).

Schoder, S. (**2023a**). "IMPLEMENTATION OF AN AEROACOUSTIC SIMULATION PIPELINE

USING OPENCFS-ACOUSTICS AND OPENCFS-DATA APPLIED TO HUMAN PHONATION," (arXiv).

Schoder, S. (**2023b**). "Offline coupling of segregated multi-physical simulations with consistent boundary conditions and source terms based on scattered data," (arXiv).

Schoder, S. (**2023c**). "OPENCFS-DATA: IMPLEMENTATION OF THE STOCHASTIC NOISE GENERATION AND RADIATION MODEL (SNGR)," (arXiv).

Schoder, S., Junger, C., and Kaltenbacher, M. (**2020**). "Computational aeroacoustics of the EAA benchmark case of an axial fan," Acta Acustica **4**.

Schoder, S., and Roppert, K. (**2022**). "OPENCFS: OPEN SOURCE FINITE ELEMENT SOFTWARE FOR COUPLED FIELD SIMULATION - PART ACOUSTICS," (arXiv).

Schoder, S., and Roppert, K. (**2023**). "OPENCFS-DATA: DATA PRE-POST-PROCESSING TOOL FOR OPENCFS," (arXiv).

Schoder, S., and Wurzinger, A. (**2023**). "Dataset CYLinCF-01 creation pipeline: Circular cylinder in a cross flow," (arXiv).

Schoder, S., Wurzinger, A., Junger, C., Weitz, M., Freidhager, C., Roppert, K., and Kaltenbacher, M. (**2021**). "Application Limits of Conservative Source Interpolation Methods Using a Low Mach Number Hybrid Aeroacoustic Workflow."

Shi, M.-S., Chi, P.-A., and Chen, W.-L. (**2019**). "Prediction on turbomachinery flows using advanced turbulence models," Journal of Aeronautics, Astronautics and Aviation **51**, 159-170.

Tomita, I., and Furukawa, M. (**2020**). "Operating range enhancement by tip leakage vortex breakdown control of a centrifugal compressor."

Vo, H. D. (**2010**). "Role of tip clearance flow in rotating instabilities and nonsynchronous vibrations," Journal of Propulsion and Power **26**, 556-561.

Wang, L., Xiang, K., Mao, L., Tong, H., and Qiao, W. (**2020**). "Numerical simulation of the effect of the tip clearance flow on rotor-stator interaction tone noise in axial-flow fan," in *ASME Turbo Expo 2020: Turbomachinery Technical Conference and Exposition, GT 2020, September 21, 2020 - September 25, 2020* (American Society of Mechanical Engineers (ASME), Virtual, Online), p. International Gas Turbine Institute.

Wei, Z., Duan, W., Qiao, W., Liu, J., and Han, P. (**2018a**). "Analysis and control of tip-leakage vortex core stability of turbine rotor," Hangkong Dongli Xuebao/Journal of Aerospace Power **33**, 2139-2149.

Wei, Z., Qiao, W., Duan, W., and Liu, J. (**2018b**). "Influence of scrapping effect on formation of casing passage vortex in turbine rotor," Hangkong Dongli Xuebao/Journal of Aerospace Power **33**, 1695-1704.

Williams, J. F., and Hawkings, D. L. (**1969**). "Sound generation by turbulence and surfaces in arbitrary motion," Philosophical Transactions for the Royal Society of London. Series A, Mathematical Physical Sciences, 321-342.

Yang, J., and Wu, H. (**2014**). "Explicit coupled solution of two-equation k- SST turbulence model and its application in turbomachinery flow simulation," Hangkong Xuebao/Acta Aeronautica et Astronautica Sinica **35**, 116-124.

Zhang, B., Mao, X., Wu, X., and Liu, B. (**2021**). "Effects of tip leakage flow on the aerodynamic performance and stability of an axial-flow transonic compressor stage," Energies **14**.

Zhang, J., Chu, W., Zhang, H., Wu, Y., and Dong, X. (**2016**). "Numerical and experimental investigations of the unsteady aerodynamics and aero-acoustics characteristics of a backward curved blade centrifugal fan," Applied Acoustics **110**, 256-267.

Zhao, H., Du, J., Zhang, W., Zhang, H., and Nie, C. (**2023**). "A review on theoretical and numerical research of axial compressor surge," Journal of Thermal Science **32**, 254-263.

Zhu, T., and Carolus, T. H. (**2018**). "Axial fan tip clearance noise: Experiments, Lattice-Boltzmann simulation, and mitigation measures," International Journal of Aeroacoustics **17**, 159-183.

Zhu, T., Lallier-Daniels, D., Sanjose, M., Moreau, S., and Carolus, T. (**2018**). "Rotating coherent flow structures as a source for narrowband tip clearance noise from axial fans," Journal of Sound and Vibration **417**, 198-215.